

Article

The K_2CO_3 – $CaCO_3$ – $MgCO_3$ System at 6 GPa: Implications for Diamond Forming Carbonatitic Melts

Anton V. Arefiev^{1,2}, Anton Shatskiy^{1,2,*}, Ivan V. Podborodnikov^{1,2} and Konstantin D. Litasov^{1,2}

¹ Department of Geology and Geophysics, Novosibirsk State University, Novosibirsk 630090, Russia; arefievanton@igm.nsc.ru (A.V.A.); podborodnikov@igm.nsc.ru (I.V.P.); klitasov@igm.nsc.ru (K.D.L.)

² Sobolev Institute of Geology and Mineralogy, Siberian Branch Russian Academy of Science, Novosibirsk 630090, Russia

* Correspondence: shatskiy@igm.nsc.ru; Tel.: +7-(383)-330-75-01

Received: 24 August 2019; Accepted: 13 September 2019; Published: 16 September 2019



Abstract: Carbonate micro inclusions with abnormally high K_2O appear in diamonds worldwide. However, the precise determination of their chemical and phase compositions is complicated due to their sub-micron size. The K_2CO_3 – $CaCO_3$ – $MgCO_3$ is the simplest system that can be used as a basis for the reconstruction of the phase composition and P – T conditions of the origin of the K-rich carbonatitic inclusions in diamonds. In this regard, this paper is concerned with the subsolidus and melting phase relations in the K_2CO_3 – $CaCO_3$ – $MgCO_3$ system established in Kawai-type multianvil experiments at 6 GPa and 900–1300 °C. At 900 °C, the system has three intermediate compounds $K_2Ca_3(CO_3)_4$ ($Ca\# \geq 97$), $K_2Ca(CO_3)_2$ ($Ca\# \geq 58$), and $K_2Mg(CO_3)_2$ ($Ca\# \leq 10$), where $Ca\# = 100Ca/(Ca + Mg)$. Miscibility gap between $K_2Ca(CO_3)_2$ and $K_2Mg(CO_3)_2$ suggest that their crystal structures differ at 6 GPa. Mg-bearing $K_2Ca(CO_3)_2$ ($Ca\# \leq 28$) disappear above 1000 °C to produce $K_2Ca_3(CO_3)_4 + K_8Ca_3(CO_3)_7 + K_2Mg(CO_3)_2$. The system has two eutectics between 1000 and 1100 °C controlled by the following melting reactions: $K_2Ca_3(CO_3)_4 + K_8Ca_3(CO_3)_7 + K_2Mg(CO_3)_2 \rightarrow [40K_2CO_3 \cdot 60(Ca_{0.70}Mg_{0.30})CO_3]$ (1st eutectic melt) and $K_8Ca_3(CO_3)_7 + K_2CO_3 + K_2Mg(CO_3)_2 \rightarrow [62K_2CO_3 \cdot 38(Ca_{0.73}Mg_{0.27})CO_3]$ (2nd eutectic melt). The projection of the K_2CO_3 – $CaCO_3$ – $MgCO_3$ liquidus surface is divided into the eight primary crystallization fields for magnesite, aragonite, dolomite, Ca-dolomite, $K_2Ca_3(CO_3)_4$, $K_8Ca_3(CO_3)_7$, $K_2Mg(CO_3)_2$, and K_2CO_3 . The temperature increase is accompanied by the sequential disappearance of crystalline phases in the following sequence: $K_8Ca_3(CO_3)_7$ (1220 °C) \rightarrow $K_2Mg(CO_3)_2$ (1250 °C) \rightarrow $K_2Ca_3(CO_3)_4$ (1350 °C) \rightarrow K_2CO_3 (1425 °C) \rightarrow dolomite (1450 °C) \rightarrow $CaCO_3$ (1660 °C) \rightarrow magnesite (1780 °C). The high $Ca\#$ of about 40 of the $K_2(Mg, Ca)(CO_3)_2$ compound found as inclusions in diamond suggest (1) its formation and entrapment by diamond under the P – T conditions of 6 GPa and 1100 °C; (2) its remelting during transport by hot kimberlite magma, and (3) repeated crystallization in inclusion that retained mantle pressure during kimberlite magma emplacement. The obtained results indicate that the K–Ca–Mg carbonate melts containing 20–40 mol% K_2CO_3 is stable under P – T conditions of 6 GPa and 1100–1200 °C corresponding to the base of the continental lithospheric mantle. It must be emphasized that the high alkali content in the carbonate melt is a necessary condition for its existence under geothermal conditions of the continental lithosphere, otherwise, it will simply freeze.

Keywords: double potassium carbonates; bütschliite; ultrapotassic carbonatite melt; high-pressure experiment; diamond formation; continental lithosphere

1. Introduction

Presence of crystalline carbonates at different mantle levels follows from the occurrence of magnesite, dolomite, calcite, and/or aragonite in spinel peridotite and eclogite xenoliths [1–3], as primary

inclusions in Cr-pyropes derived from 100–130 km depth [4,5], and as inclusions in diamonds derived from the base of the continental lithosphere and deeper levels [6–13]. Ca-Mg carbonates also appear as rock-forming minerals and/or as inclusions in high-pressure minerals in diamondiferous ultrahigh-pressure (UHP) metamorphic rocks exhumed from 150–250 km depths [14–17].

A number of studies of ‘fibrous’ diamonds (diamonds with high dislocation density) from kimberlites worldwide revealed the presence of K-rich carbonatitic melt inclusions coexisting with both peridotitic and eclogitic minerals [18–25]. The inclusions retain high internal pressure suggesting the mantle origin of the entrapped melt [26]. Recently this melt was also found as micro inclusions in the central part of a gem-quality diamond crystal [27] and along the twinning plane in ancient diamonds [28]. This suggests that alkali-rich carbonate melts have been introduced into the reduced lithospheric mantle since the Archaean and that these melts could be responsible for the formation of most lithospheric diamonds [28].

It was shown experimentally that the upper mantle K-rich carbonate melts could be formed by partial melting of carbonated pelites [29–31] at pressures of 5–8 GPa. However, precise determination of the compositions of these melts and subsolidus phases controlling melting reactions in the complex natural-like systems with realistic bulk compositions involving small proportions of CO₂ is problematic due to their trace amounts and the lack of stability of quenched products during polishing and electron probe microanalysis [32]. It is also difficult to determine the true position of the solidus lines in the *P*–*T* space.

In contrast, the study of pure carbonate systems allows careful determination of subsolidus carbonate phases, minimum melting temperatures, and the composition of incipient melt, which facilitate the interpretation of the natural-like carbonate-bearing silicate systems.

The study of the K₂CO₃–CaCO₃–MgCO₃ system at 6 GPa was initiated by Shatskiy, et al. [33], who examined a binary K₂CO₃–Ca_{0.5}Mg_{0.5}–(CO₃)₂ join. In the present work, we carried out a full study of the K₂CO₃–CaCO₃–MgCO₃ phase diagram involving an incomparably larger number of experimental points collected at 6 GPa in the range of 900–1300 °C (Tables S1–S9).

2. Materials and Methods

Experiments were performed in a ‘Discoverer-1500’ DIA-type multianvil apparatus at IGM SB RAS in Novosibirsk, Russia. The inner stage of anvils consisted of eight 26 mm tungsten carbide cubes, ‘Fujillo N-05’, with 12 mm truncations. ZrO₂ pressure media (OZ-8C, MinoYogyo Co., Ltd [34]) was shaped as a 20.5 mm octahedron with ground edges and corners. A multi-charge assembly allowed simultaneous loading of up to 16 samples [35]. The temperature was measured by a W₉₇Re₃–W₇₅Re₂₅ thermocouple and controlled automatically within 2.0 °C of the target value. The thermocouple junction was located at the heater center in the high-temperature (HT) zone. Maximum thermal gradient across the sample charge did not exceed 5–8 °C/mm at 900–1300 °C [35,36]. Uncertainty in the temperature and pressure estimates are less than 20 °C and 0.5 GPa, respectively. The cell assembly design, pressure calibration, and temperature distribution across sample charge are given in [35,36].

Since the studied system includes highly hygroscopic K₂CO₃, special care was taken to avoid the contamination of the samples by water before the experiment and to prevent damage of the post-experimental samples by atmospheric humidity during polishing. K₂CO₃-bearing samples easily absorb water from the atmospheric air. Placing the sample in a vacuum for carbon coating results in water evaporation and precipitation of needle crystals of K-phase, presumably KHCO₃, on the sample surface. This prevents the chemical analysis of the obtained phases. Examples of BSE images of well-polished samples and the same samples damaged by atmospheric humidity are shown in Figure S1. The procedures of the sample preparation and polishing are described in [31,37].

Recovered samples were studied using a MIRA 3 LMU scanning electron microscope (Tescan Orsay Holding, Brno, Czech) coupled with an INCA energy-dispersive X-ray microanalysis system 450 equipped with the liquid nitrogen-free Large area EDS X-Max-80 Silicon Drift Detector (Oxford Instruments Nanoanalysis Ltd, Oxford, UK) at IGM SB RAS (see [37] for details).

3. Experimental Results

The results of the experiments in the system K_2CO_3 – $CaCO_3$ – $MgCO_3$ including phase compositions of recovered samples and chemical compositions of obtained carbonate phases are summarized in Tables S1–S9. Backscattered electron (BSE) images of experimental samples are shown in Figures 1–4. The isothermal sections of the T - X ternary diagram are shown in Figure 5. A list of abbreviations is given in the Nomenclature section.

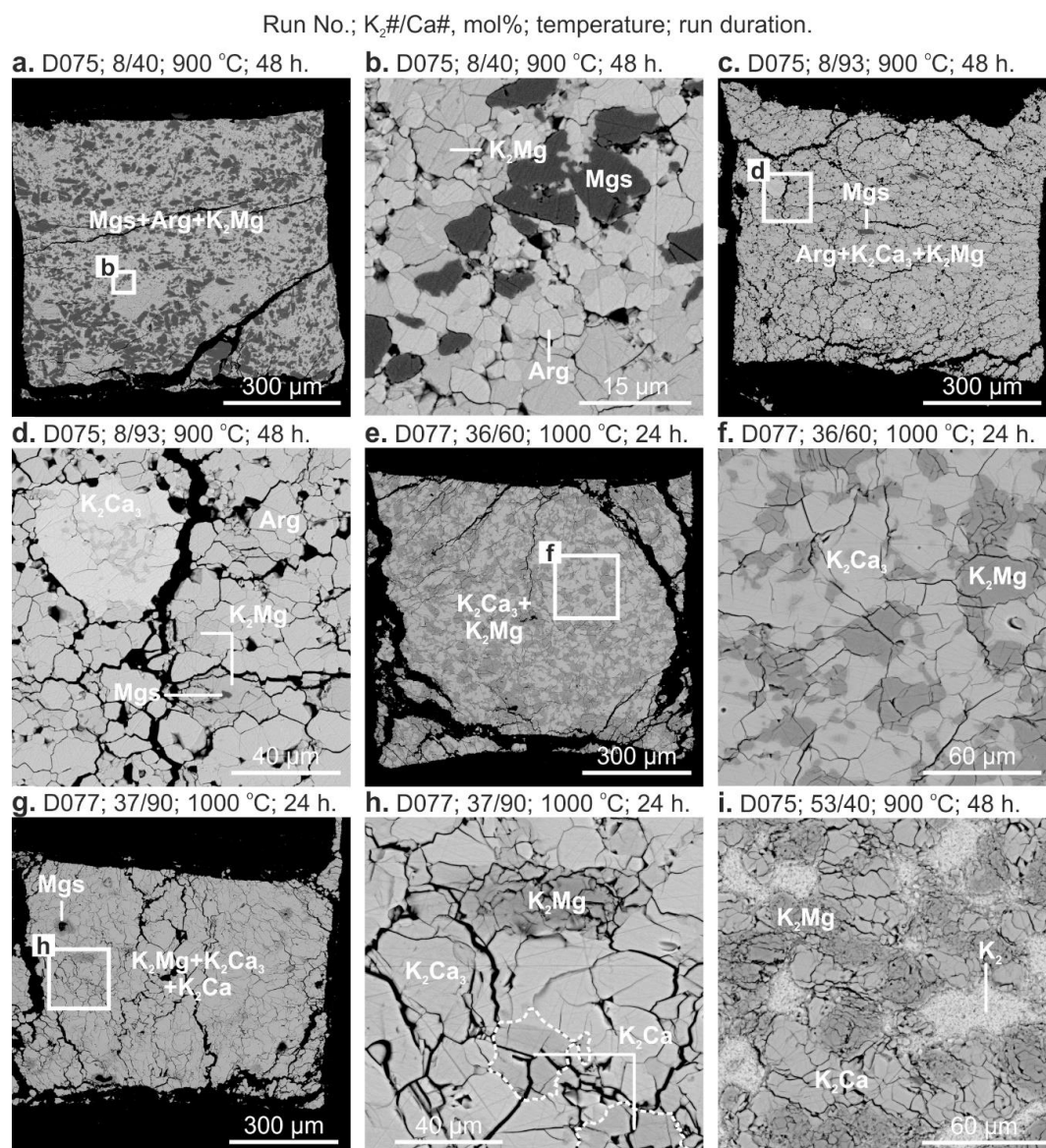


Figure 1. Backscattered electron (BSE) images of sample cross-sections illustrating subsolidus phase relationships in the system K_2CO_3 – $CaCO_3$ – $MgCO_3$ at 6 GPa. The samples represent two runs: D075 at 900 °C with a duration of 48 h (a–d,i); D077 at 1000 °C and 24 h (e–h). $K_2\#/Ca\#$ indicates bulk composition of the starting mixture, $K_2\# = 100 \cdot K_2CO_3 / (K_2CO_3 + CaCO_3 + MgCO_3)$, $Ca\# = 100 \cdot CaCO_3 / (CaCO_3 + MgCO_3)$. See the Nomenclature section for abbreviations.

At 900 °C (run D075, 48 h) and 1000 °C (run D077, 24 h), the run products are represented by subsolidus phase assemblages (Figure 5a,b). Typically, the limiting reagents have been consumed completely. However, in some runs, the relicts of MgS were observed among the run products (Figure 1c,d,g). At these temperatures, three intermediate compounds, K_2Mg , K_2Ca , and K_2Ca_3 , were found. Their stoichiometries resemble those in the corresponding binary systems [36,38]. The K_2Ca_3

and K_2Ca compounds dissolve up to 7 and 30–40 mol% of Mg components, respectively, whereas K_2Mg dissolves up to 17 mol% of Ca component (Tables S1 and S2). The compositions of these compounds can be approximated as follows: $K_2(Ca_{\geq 0.93}Mg_{\leq 0.07})_3(CO_3)_4$, $K_2(Ca_{\geq 0.58}Mg_{\leq 0.42})(CO_3)_2$, and $K_2(Mg_{\geq 0.83}Ca_{\leq 0.17})(CO_3)_2$ (Tables S1 and S2). Although a mutual solubility of K_2Mg and K_2Ca compounds is noticeable, a miscibility gap between these phases was observed (Figures 1i and 5a,b, and Tables S1 and S2). It was previously shown that at 6 GPa, $K_2Ca(CO_3)_2$ bütschliite decomposes between 950 and 1000 °C according to the reaction [38,39]:



Our results suggest that the partial substitution of Ca with Mg extends its stability to 1000 °C (Figure 5b). K_2CO_3 dissolves up to 2 mol% $CaCO_3$ and minor amounts of $MgCO_3$ (Figure 5a,b, Tables S1 and S2).

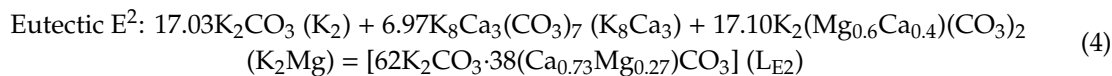
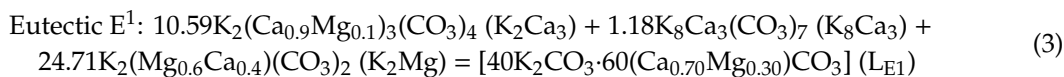
The following three-phase regions were established at 900 and 1000 °C (Figure 5a,b): $Mgs + Arg + K_2Mg$ (Figure 1a,b), $Arg + K_2Ca_3 + K_2Mg$ (Figure 1c,d), $K_2Mg + K_2Ca_3 + K_2Ca$ (Figure 1g,h), and $K_2 + K_2Mg + K_2Ca$ (Figure 1i), while the two-phase fields include $Arg + K_2Ca_3$, $Arg + K_2Mg$, $K_2Ca_3 + K_2Ca$, $K_2Ca_3 + K_2Mg$ (Figure 1e,f), $K_2Ca + K_2$, $K_2Ca + K_2Mg$, $Mgs + K_2Mg$, and $K_2Mg + K_2$. According to the phase relations established in the binary K_2CO_3 – $CaCO_3$ system, K_8Ca_3 compound is stable at 900 °C and disappears via congruent melting above 1200 °C [38]. This suggests the existence of narrow three- and two-phase fields containing K_8Ca_3 (Figure 5a,b).

As temperature increases to 1100 °C (runs D078, 47 h and D158, 6 h), the diagram undergoes significant changes including an appearance of two liquid fields, $K_8(Ca_{\geq 0.97}Mg_{\leq 0.03})_3(CO_3)_7$, and Ca-Dol (Ca# 5–7) and disappearance of Mg-bearing K_2Ca (Figure 5e, Tables S3 and S4). The appearance of Ca-Dol is consistent with the phase relations established in the $CaCO_3$ – $MgCO_3$ system [35]. The isothermal section contains two subsolidus three-phase fields: $Mgs + K_2Ca_3 + Dol$ (Figure 2a), $Arg + K_2Ca_3 + Ca-Dol$ (Figure 2b) and five subsolidus two-phase fields: $Arg + K_2Ca_3$, $K_2Ca_3 + K_8Ca_3$, $K_8Ca_3 + K_2$, $Dol + K_2Ca_3$, $Mgs + K_2Mg$, and $K_2Mg + K_2$ (Figure 5e). One liquid field is surrounded by four two-phase fields: $K_2Ca_3 + L_{E1}$, $K_8Ca_3 + L_{E1}$, $K_2Mg + L_{E1}$, (Figure 2f,i), and $Mgs + L_{E1}$ and four three-phase fields: $K_2Ca_3 + K_8Ca_3 + L_{E1}$ (Figure 2h), $K_8Ca_3 + K_2Ca + L_{E1}$, $K_2Mg + Mgs + L_{E1}$ (Figure 2c,e), and $Mgs + Dol + L_{E1}$ (Figure 5e). At 1100 °C, the L_{E1} composition varies in the range of 32–54 mol% K_2CO_3 and Ca# = 56–84 mol% (Figure 5e and Tables S3 and S4). Another liquid field is surrounded by three two-phase fields including $K_8Ca_3 + L_{E2}$ (Figure 2j), $K_2 + L$ (Figure 2l), and $K_2Mg + L$ and three three-phase fields: $K_8Ca_3 + K_2 + L_{E2}$ (Figure 2k), $K_2 + K_2Mg + L_{E2}$, and $K_2Mg + K_8Ca_3 + L_{E2}$ (Figure 5e). In this field, the melt composition L_{E2} varies in the range of 57–66 mol% K_2CO_3 and Ca# = 45–84 mol%.

Some samples recovered from the 1100 °C experiments contain subsolidus assemblages at their low-temperature (LT) side. Given the thermal gradient across the sample charge, 6–7 °C/mm at 1100 °C, and the longest distance from the thermocouple junction to the sample end, 2.5–3.0 mm, the temperature at the LT side was about 1080 °C in the runs at 1100 °C. Phase relations inferred from the LT samples sides are shown in Figure 5c. The results suggest that temperature increase from 1000 to 1080 °C, the $Arg + K_2Mg$ assemblage becomes prohibited owing to the following subsolidus reaction:



Reaction (2) changes subsolidus assemblages in the join Mgs – Arg – K_2Ca_3 – K_2Mg and yields an appearance of the following three-phase fields: $K_2Mg + Mgs + K_2Ca_3$ (Figure 2c,d), $Mgs + Dol + K_2Ca_3$ (Figure 2a), and $Ca-Dol + Arg + K_2Ca_3$ (Figures 2b and 5c). Considering subsolidus phase relations at ~1080 °C (Figure 5c) and melting phase relations at 1100 °C (Figure 5e), the system has two eutectics controlled by the following four-phase reactions (Figure 5d and Table S10).



Run No.; K₂#/Ca#, mol%; temperature; run duration.

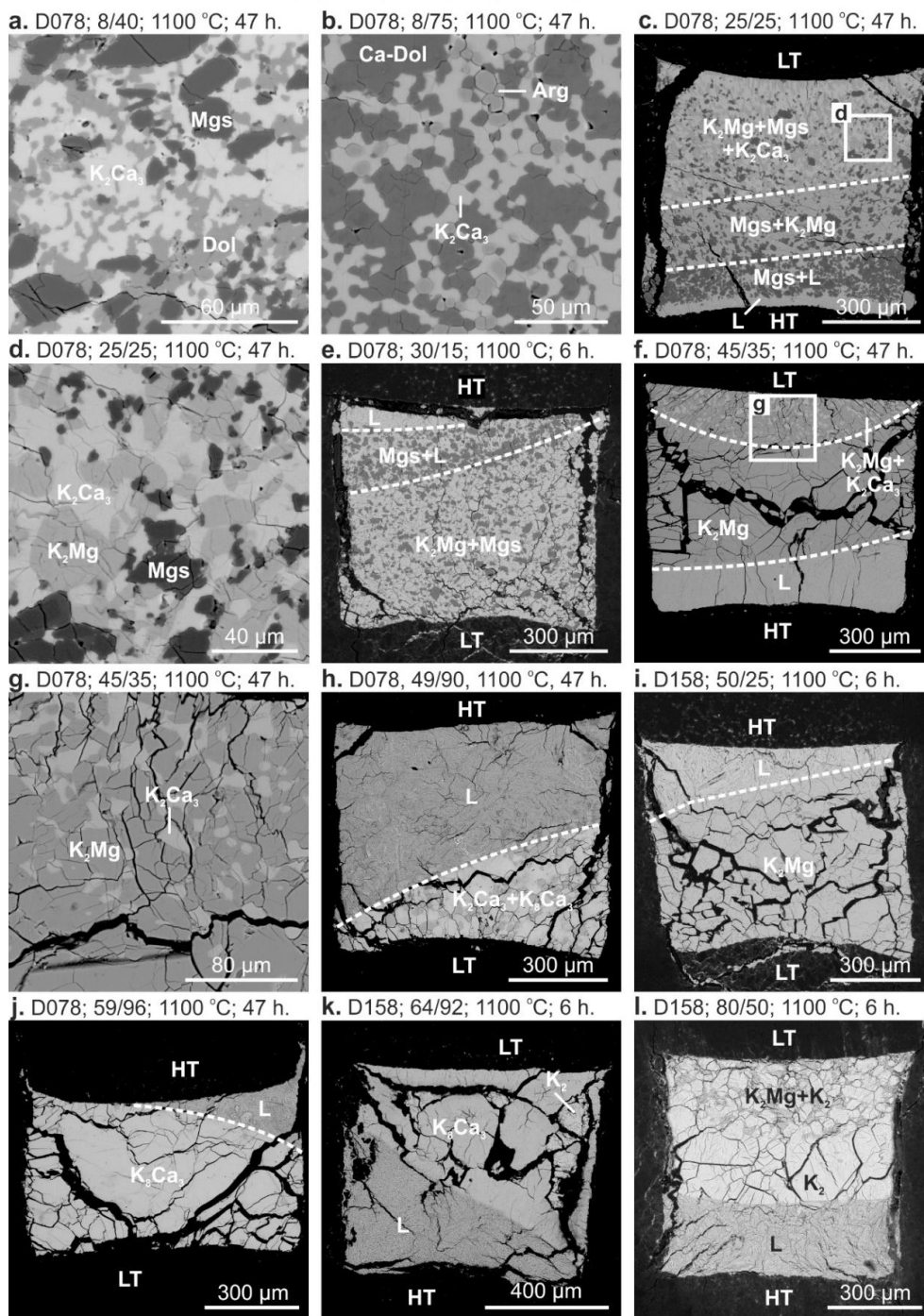


Figure 2. BSE images of sample cross-sections illustrating phase relationships in the system $\text{K}_2\text{CO}_3\text{--CaCO}_3\text{--MgCO}_3$ at 6 GPa and 1100 °C. $\text{K}_2\#\text{/Ca}\#$ indicates bulk composition of the starting mixture, $\text{K}_2\# = 100 \cdot \text{K}_2\text{CO}_3 / (\text{K}_2\text{CO}_3 + \text{CaCO}_3 + \text{MgCO}_3)$, $\text{Ca}\# = 100 \cdot \text{CaCO}_3 / (\text{CaCO}_3 + \text{MgCO}_3)$. LT—low-temperature side. HT—high-temperature side. See the Nomenclature section for abbreviations.

Run No.; $K_2\#/Ca\#$, mol%; temperature; run duration.

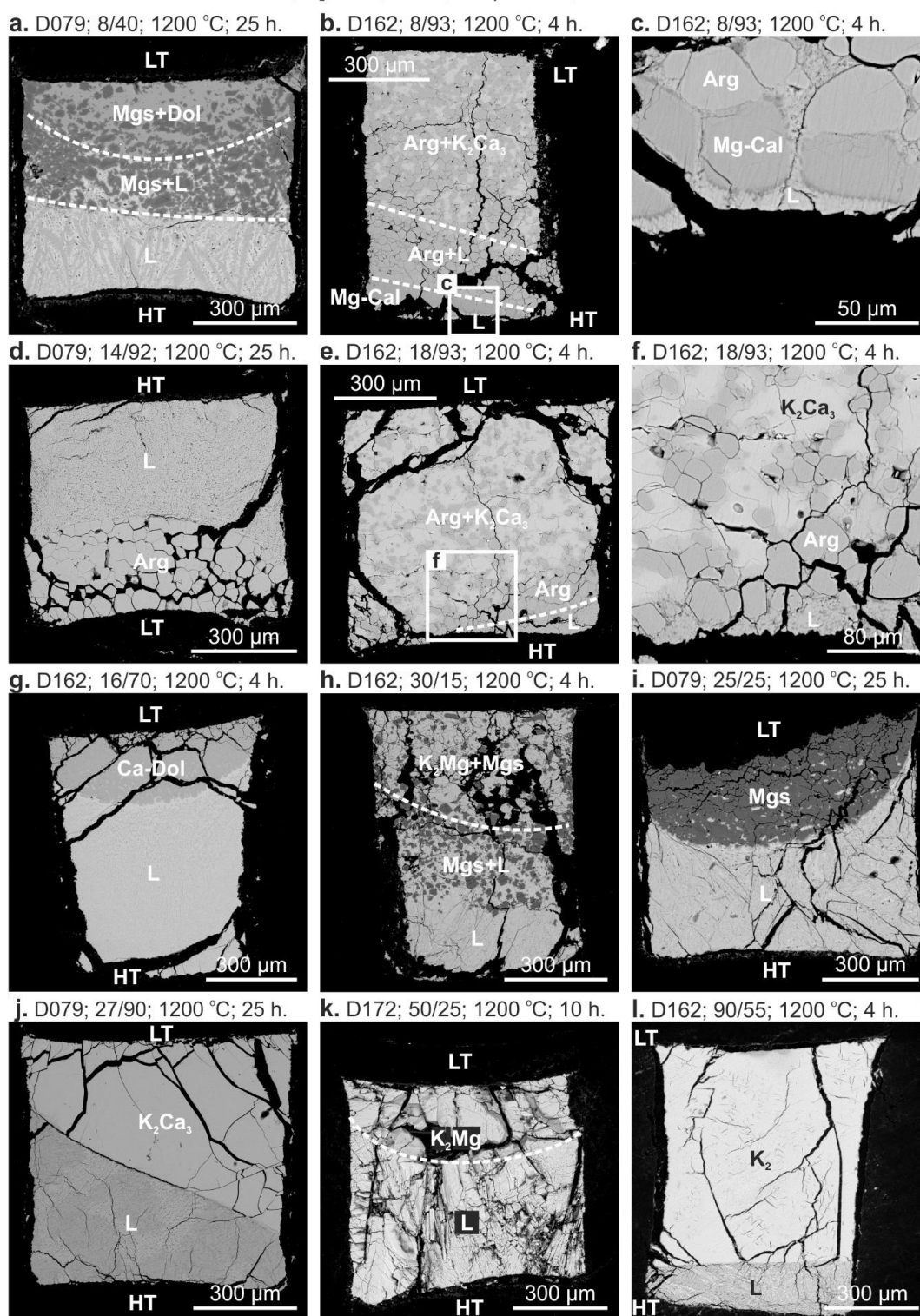


Figure 3. BSE images of sample cross-sections illustrating phase relationships in the system K_2CO_3 – $CaCO_3$ – $MgCO_3$ at 6 GPa and 1200 °C. $K_2\#/Ca\#$ indicates bulk compositions of the starting mixtures, $K_2\# = 100 \cdot K_2CO_3 / (K_2CO_3 + CaCO_3 + MgCO_3)$, $Ca\# = 100 \cdot CaCO_3 / (CaCO_3 + MgCO_3)$. LT—low-temperature side. HT—high-temperature side. See the Nomenclature section for abbreviations.

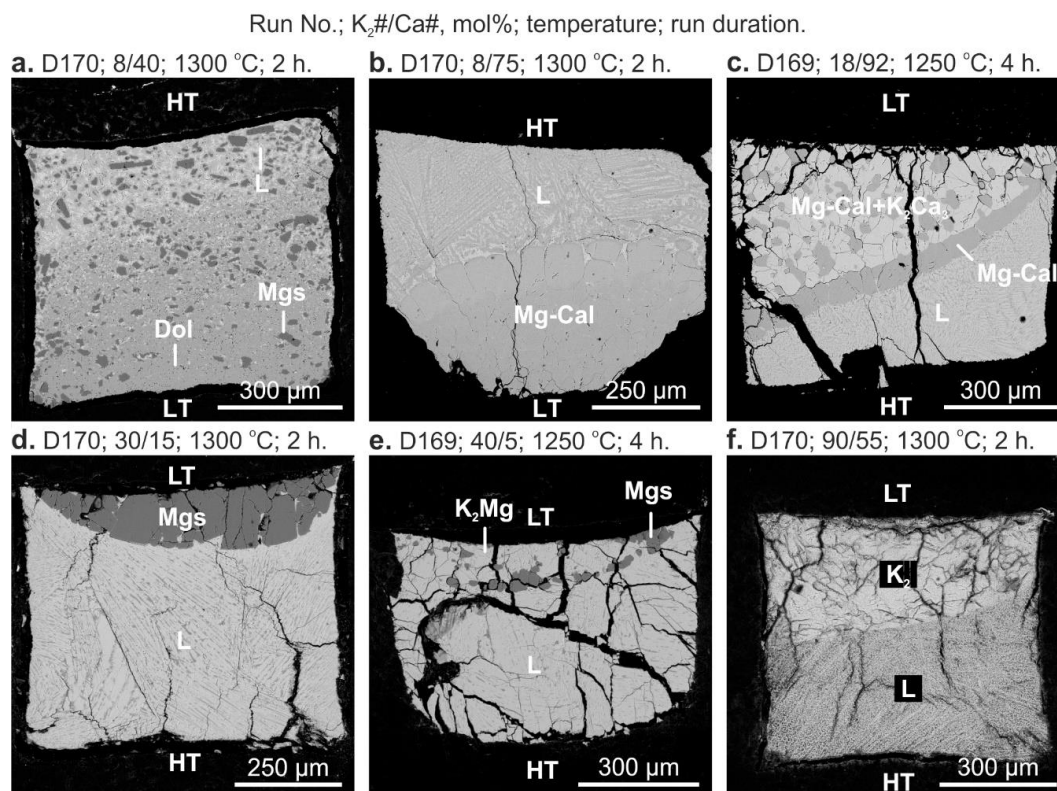


Figure 4. BSE images of sample cross-sections illustrating phase relationships in the system $\text{K}_2\text{CO}_3\text{--CaCO}_3\text{--MgCO}_3$ at 6 GPa and 1250–1300 °C. $K_2\#/\text{Ca}\#$ indicates bulk composition of the starting mixture, $K_2\# = 100 \cdot \text{K}_2\text{CO}_3 / (\text{K}_2\text{CO}_3 + \text{CaCO}_3 + \text{MgCO}_3)$, $\text{Ca}\# = 100 \cdot \text{CaCO}_3 / (\text{CaCO}_3 + \text{MgCO}_3)$. LT—low-temperature side. HT—high-temperature side. See the Nomenclature section for abbreviations.

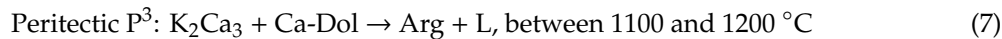
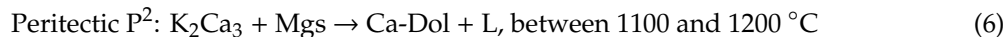
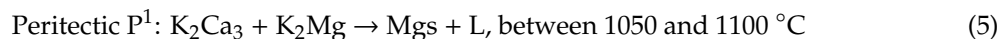
As temperature increases to 1200 °C (runs D079, 25 h; D162, 4 h; D162, 10 h), the liquid fields remarkably expand and combine into a single one (Figure 5f). This field is surrounded by seven two-phase fields: Mgs + L (Figure 3i), Dol + L (Figure 3g), Arg + L (Figure 3d), K_2Ca_3 + L (Figure 3j), K_8Ca_3 + L, K_2 + L (Figure 3l), K_2Mg + L (Figure 3k) and four three-phase fields: K_2Mg + Mgs + L (Figure 3h), Mgs + Dol + L (Figure 3a), Mg-Cal + Arg + L (Figure 3b,c), Arg + K_2Ca_3 + L (Figure 3e,f).

With a further increase in temperature, the melt region continues to expand, while the number of two-phase and three-phase fields decreases (Figure 5g,h). At 1250 °C (run D169, 4 h), the K_8Ca_3 + L and Mgs + K_2Mg fields disappear. The isothermal section includes seven two-phase fields: Mgs + L, Dol + L, Arg + L, Arg + K_2Ca_3 , K_2Ca_3 + L, K_2 + L, K_2Mg + L and four three-phase fields: K_2Mg + Mgs + L (Figure 4e), Mgs + Dol + L, Mg-Cal + Arg + L, Arg + K_2Ca_3 + L (Figure 4c). Most of these fields remain at 1300 °C (run D170, 2 h), such as Mgs + L (Figure 3d), Dol + L (Figure 3b), K_2 + L (Figure 3f), Mgs + Dol + L (Figure 4a), while the Arg + K_2Ca_3 , Arg + K_2Ca_3 + L, K_2Mg + L, and K_2Mg + Mgs + L disappear (Figure 5h).

Regardless of the temperature and the composition of the starting mixture, the maximum CaCO_3 and MgCO_3 contents established in potassium carbonate are less than 3 and 1 mol%, respectively (Figure 5 and Tables S1–S9). The K_2CO_3 content in alkaline earth carbonates (aragonite, calcite, calcite-dolomite solid solutions, and magnesite) varies within the uncertainty of our EDS measurements (i.e., <0.5 mol%) (Tables S1–S9).

Liquidus phase relations in the $\text{K}_2\text{CO}_3\text{--CaCO}_3\text{--MgCO}_3$ system are illustrated in Figure 6. There are eight primary solidification phase fields characterized by the initial crystallization of Mgs (Figures 3i and 4d), Arg (Figure 3d), Dol, Ca-Dol (Figures 3g and 4b), K_2Ca_3 (Figure 3j), K_8Ca_3 (Figure 2j),

K_2Mg (Figures 2i and 3k), and K_2 (Figures 2l, 3l and 4f). The system has four ternary peritectic points, controlled by the following reactions:



and two eutectic points (E¹ and E²) located just below 1100 °C and controlled by Reactions (3) and (4), respectively (Figure 6).

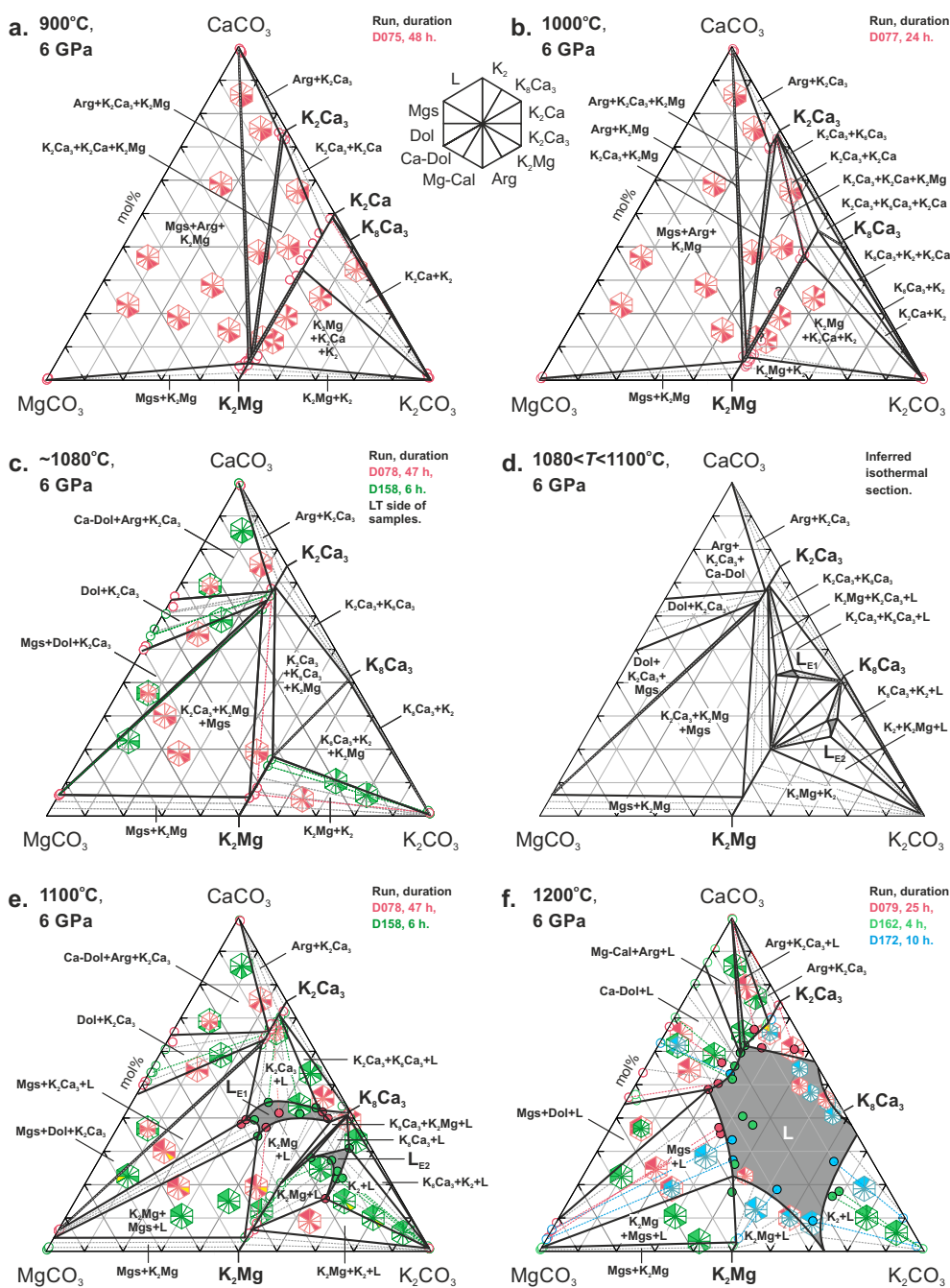


Figure 5. Cont.

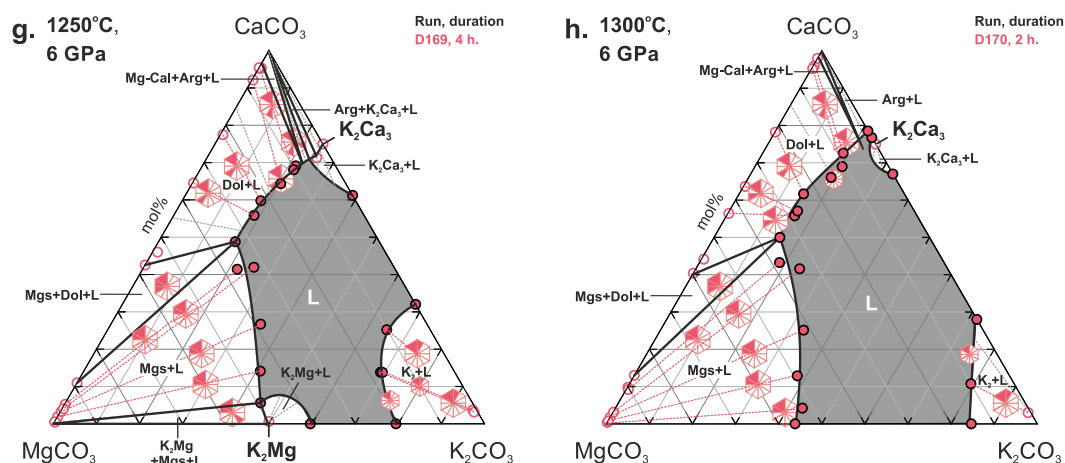


Figure 5. Isothermal sections of the K_2CO_3 – $MgCO_3$ – $CaCO_3$ T - X diagram at 6 GPa. (a) 900 °C, (b) 1000 °C, (c) ~1080 °C, (d) 1080 < T < 1100 °C (inferred), (e) 1100 °C, (f) 1200 °C, (g) 1250 °C, (h) 1300 °C. $K_2 = K_2CO_3$, $K_8Ca_3 = K_8Ca_3(CO_3)_7$ ($Ca\# \geq 97$), $K_2Ca = K_2(Ca,Mg)(CO_3)_2$ ($Ca\# \geq 51$), $K_2Ca_3 = K_2Ca_3(CO_3)_4$ ($Ca\# \geq 93$), $K_2Mg = K_2Mg(CO_3)_2$ ($Ca\# \leq 42$), Arg = aragonite, Ca-Dol = Ca-rich dolomite, Dol = dolomite, Mg-Cal = Mg-bearing calcite, Mgs = magnesite, L = liquid. Colored marks denote different runs shown in the upper-right corner of each isothermal section. Open and filled circles indicate the compositions of solid and liquid phases measured by EDS. Filled segments in hexagons denote phases present. Yellow segments indicate the phases appearing in the LT side.

4. Discussion

4.1. Comparison with the Previous Study

Shatskiy et al. [33] determined the phase relations along the K_2CO_3 – $Ca_{0.5}Mg_{0.5}CO_3$ join at 6 GPa using an experimental and analytical technique similar to the present study. Although a number of experimental points in their study were very limited, they succeeded to infer a few phase fields, Arg + K_2Mg , $K_2Mg + K_2$, Mgs + K_2Mg , and Arg + $K_2Mg + Mgs$ at 900 °C (Figure 3a in their study) like those established in the present study (Figure 5a). They also observed two distinct compositions of the $K_2(Mg, Ca)(CO_3)_2$ compound with Ca# of ~10 and 50–58 and interpreted them as solid solution series, i.e., as a single phase (Figure 3a in their study). Yet, based on the present results these compounds are immiscible under the specified P – T conditions (Figure 5a).

They also found two minima on the liquidus surface (Figure 3a in their study), whose compositions resemble those established in the present study, and succeeded to establish the Mgs + L, $K_2Mg + Mgs + L$, and $K_2Mg + L$ fields (Figure 3b in their study) (Figure 5b). Given the temperature step of 100 °C in both studies, slightly lower minimum melting temperatures, 1000 °C instead of 1080 °C in the present study, is not surprising.

The experimental points obtained by Shatskiy et al. [33] at 1100 and 1200 °C (Figure 3c,d in their study) are in reasonable agreement with those obtained in the present study (Figure 5e,f). The difference in some details of their interpretation is rather associated with an insufficient number of experimental points in their study [33] than with the inconsistency in the experimental data. For instance, Shatskiy, et al. [33] have interpreted the first melt $[36K_2CO_3 \cdot 64(Ca_{0.65}Mg_{0.35})CO_3]$, found in coexistence with Mgs and K_2Mg at 1000 °C as a eutectics. However, according to present results, the melt with such composition and coexisting phases is generated by peritectic reaction 5 (P^1 in Figure 6).

4.2. Effect of Pressure

Under mantle pressures and temperatures, the K_2CO_3 – $CaCO_3$ – $MgCO_3$ system (KCM) forms several intermediate compounds represented by alkali-alkaline earth double carbonates. At 3 GPa and 750 °C, these carbonates are represented by the low-pressure phases including $K_2Mg(CO_3)_2$, $K_2Ca_2(CO_3)_2$, and $K_2Ca(CO_3)_2$ bütschliite [37,39,40] (Figure 7a,b), which are also stable at ambient

pressure [41–43]. At 6 GPa, K_2Mg remains stable up to 1250 °C, where it melts congruently [40], while the stability field of K_2Ca is limited by ~990 °C for the pure endmember (Figure 6) [39] and ~1050 °C for the Mg-bearing compound (Figure 5d,c). The decomposition of K_2Ca yields formation of high-pressure carbonates including $K_8Ca_3 + K_2Ca_3 \pm K_2Mg$ (Figure 7d). Thus, at 6 GPa and 1080 °C, the intermediate compounds are represented by K_2Mg , K_2Ca_3 , K_8Ca_3 , and Dol (Figure 5d).

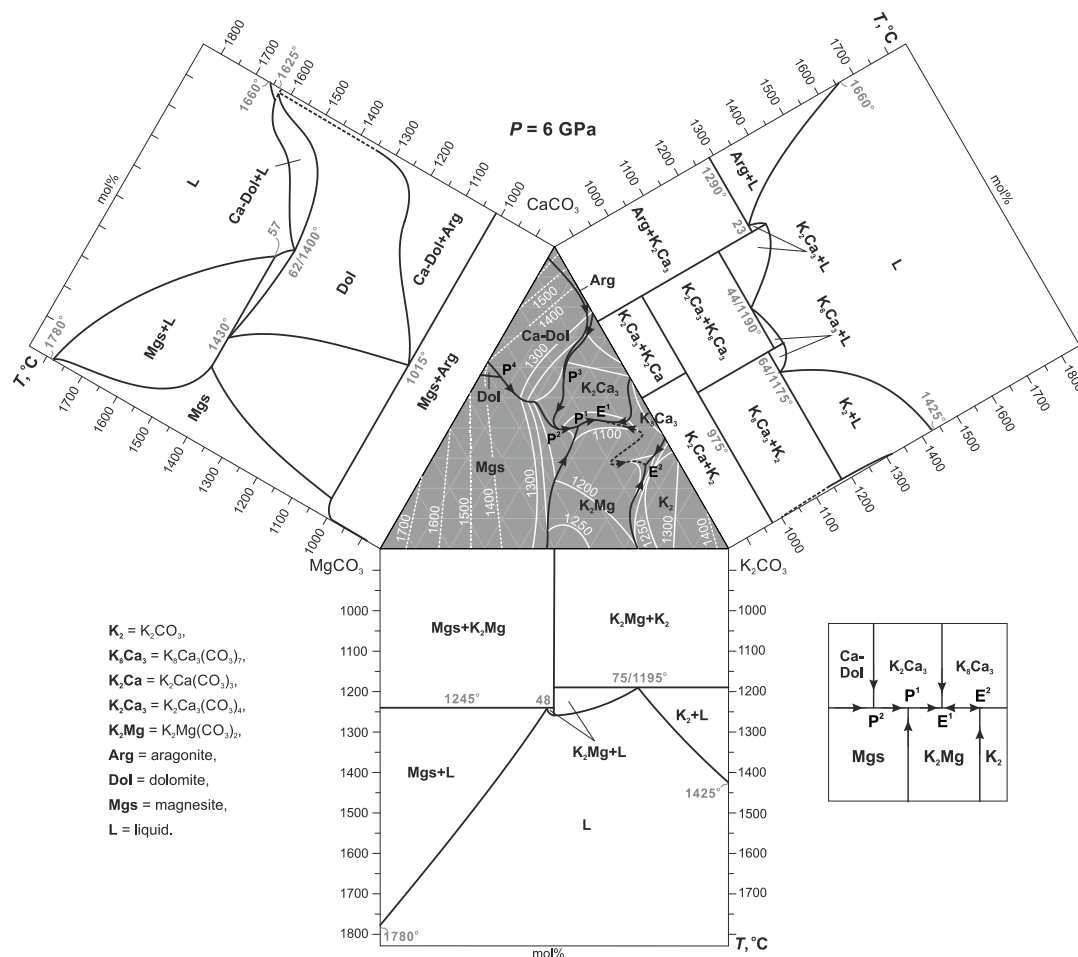


Figure 6. Liquidus phase relations in the system K_2CO_3 – $MgCO_3$ – $CaCO_3$ at 6 GPa. Black are boundary lines and white lines are liquidus isotherms with temperatures in degrees Celsius. Dashed lines were inferred. The phase relations in the corresponding binaries are from [35,36,38,43]. The relative position of peritectic and eutectic points is shown on the schematic sketch at the right-bottom. See the Nomenclature section for abbreviations.

At 3 GPa, the diagram has one minimum on the liquidus surface, which is a K_2 – K_2Mg – K_2Ca ternary eutectic located at $53K_2CO_3 \cdot 47Ca_{0.4}Mg_{0.6}CO_3$ and ~825 °C (Figures 7b and 8a). The present study showed that at 6 GPa, the system has two minima corresponding to K_2Ca_3 – K_8Ca_3 – K_2Mg and K_8Ca_3 – K_2 – K_2Mg eutectics at $40K_2CO_3 \cdot 60(Ca_{0.70}Mg_{0.30})CO_3$ and $62K_2CO_3 \cdot 38(Ca_{0.73}Mg_{0.27})CO_3$, respectively. Both are located at 1090 °C (Figures 7d and 8b). See the Nomenclature section for abbreviations.

4.3. Comparison with the Na-Bearing System

Similar to KCM at 6 GPa, the Na_2CO_3 – $CaCO_3$ – $MgCO_3$ system (NCM) forms several intermediate compounds including Dol, Na_2Ca_4 , Na_2Ca_3 , Na_4Ca , and Na_2Mg [44]. The first melting occurs at 1050 °C, which is close to that in KCM (1090 °C). In contrast to KCM (Figure 8b), which has two eutectics, NCM has a single eutectic, Na_2Ca_3 – Na_4Ca – Na_2Mg , with a composition of $48Na_2CO_3 \cdot 52(Ca_{0.75}Mg_{0.25})CO_3$

(Figure 8d). As pressure decreases to 3 GPa, the incipient melting of NCM shifts to 850 °C and controlled by the $\text{Na}_2\text{Ca} + \text{Na}_2 + \text{Na}_2\text{Mg}$ assemblage [45], similar to the $\text{K}_2\text{Ca}-\text{K}_2-\text{K}_2\text{Mg}$ eutectic established in KCM at 3 GPa and 825 °C [37] (Figure 8a,c). The difference is that the KCM eutectic is Mg-rich, $53\text{K}_2\text{CO}_3\cdot 47\text{Ca}_{0.4}\text{Mg}_{0.6}\text{CO}_3$, while the NCM eutectic is Ca-rich with compositions of $52\text{Na}_2\text{CO}_3\cdot 48\text{Ca}_{0.62}\text{Mg}_{0.38}\text{CO}_3$ (Figure 8a,c).

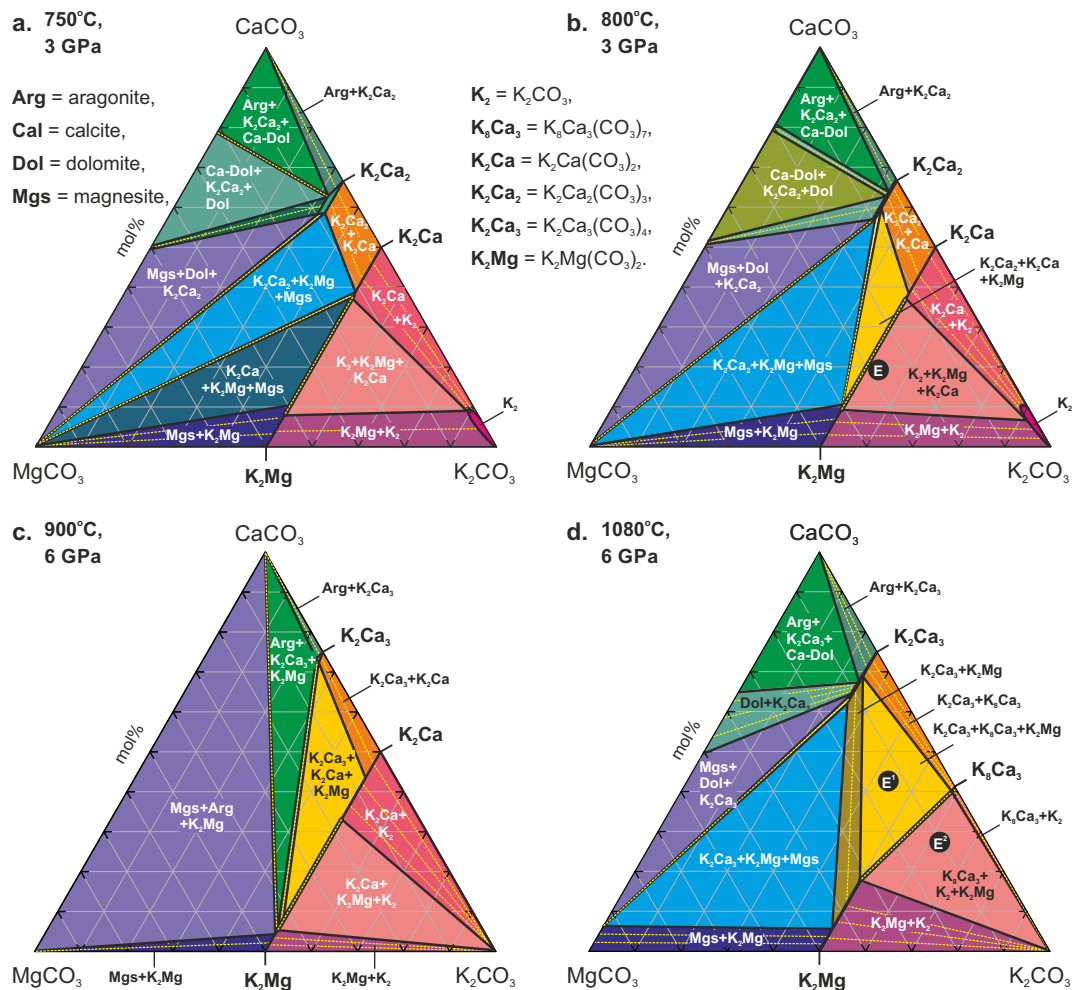


Figure 7. Isothermal and isobaric sections of the K_2CO_3 – CaCO_3 – MgCO_3 T - X diagram at 3 GPa, 750 °C (a) and 800 °C (b) [37] and at 6 GPa, 900 °C (c) and 1080 °C (d) (this study). E, E¹, and E² denote corresponding eutectic points. See the Nomenclature section for abbreviations.

4.4. Mutual Solubility of $\text{K}_2\text{Ca}(\text{CO}_3)_2$ and $\text{K}_2\text{Mg}(\text{CO}_3)_2$

Carbonate with the $\text{K}_2\text{Mg}(\text{CO}_3)_2$ stoichiometry was first synthesized at 4 MPa [46] and then was also obtained under the upper mantle and even transitions zone P – T conditions [32,36,40,47]. The crystal structure analysis performed at ambient conditions revealed that $\text{K}_2\text{Mg}(\text{CO}_3)_2$ is isostructural to $\text{K}_2\text{Ca}(\text{CO}_3)_2$ bütschliite [48] and has the rhombohedral symmetry with the space group $R\bar{3}m$ [49]. In situ X-ray diffraction study revealed that $\text{K}_2\text{Mg}(\text{CO}_3)_2$ retains its structure to 8 GPa upon compression at the ambient temperature where it transforms into a monoclinic polymorph [50]. However, the present results at 6 GPa and the results at 3 GPa [37] show a miscibility gap on the $\text{K}_2\text{Ca}(\text{CO}_3)_2$ – $\text{K}_2\text{Mg}(\text{CO}_3)_2$ join (Figure 7a–c). This suggests that crystal structures of $\text{K}_2\text{Mg}(\text{CO}_3)_2$ and $\text{K}_2\text{Ca}(\text{CO}_3)_2$ at 3–6 GPa and 750–1000 °C are different. Indeed, X-ray diffraction patterns taken from $\text{K}_2\text{Mg}(\text{CO}_3)_2$ in situ in HP-HT experiments revealed that the crystal structure of $\text{K}_2\text{Mg}(\text{CO}_3)_2$ at 6.5 GPa and 1000 °C and at 1.1 GPa and 400 °C differs from bütschliite [36].

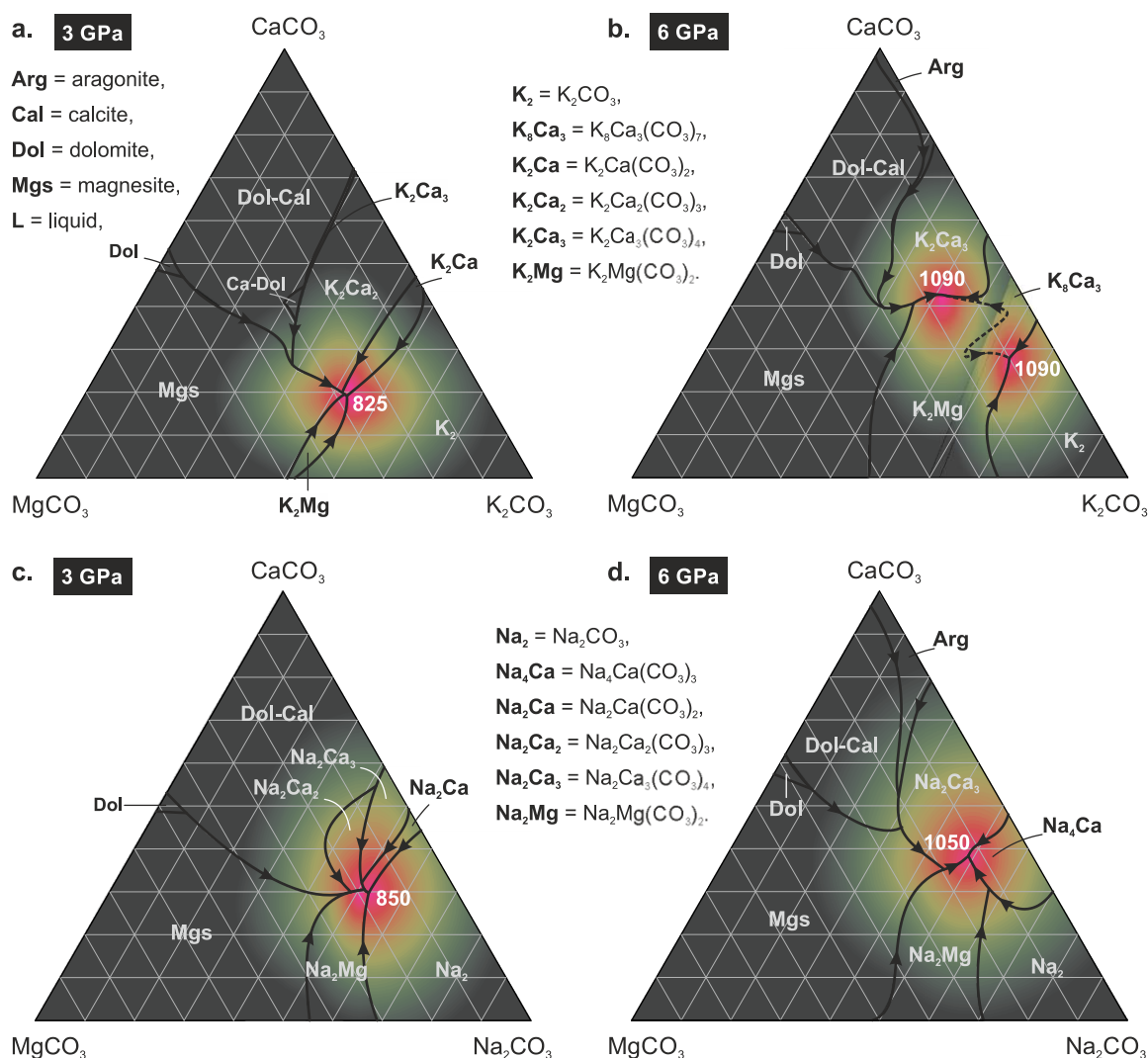


Figure 8. The diagrams illustrating primary crystallization regions and ternary eutectics in the system K_2CO_3 – $CaCO_3$ – $MgCO_3$ at 3 GPa (a) [37] and at 6 GPa (b) (this study) and in the system Na_2CO_3 – $CaCO_3$ – $MgCO_3$ at 3 GPa (c) [45] and at 6 GPa (d) [44]. Na_2 — Na_2CO_3 , Na_2Ca_2 — $Na_2Ca_2(CO_3)_3$, Na_2Ca_3 — $Na_2Ca_3(CO_3)_4$, Na_2Mg — $Na_2Mg(CO_3)_2$, see the Nomenclature section for other abbreviations.

4.5. Variety of Carbonates in Diamonds and Their Origin

A wide range of carbonates has been detected among inclusions in diamonds: magnesite [7,8], dolomite [9,11,24,51], calcite [6,11], aragonite [12], siderite [52], and various alkali-bearing double carbonates: $K_2Ca(CO_3)_2$ bütschliite [27], $K_2(Mg_{0.9-0.5}Ca_{0.1-0.5})(CO_3)_2$ [28], $(Na, K)_2Ca(CO_3)_2$ nyerereite [53], and $Na_2Mg(CO_3)_2$ eitelite [54,55]. The origin of carbonate minerals in the syngenetic inclusions in diamonds can be different. Some of them could be entrapped as minerals crystallized syngenetically with the host diamond from carbonatite melt. Others could be the daughter phases, precipitated from the entrapped melt during kimberlite magma emplacement and cooling. Below, we discuss a possible origin of various carbonate minerals found in diamonds considering the established phase relations in KCM and NCM systems.

It is generally accepted that most diamonds were crystallized at the base of ancient cratons at 5–7 GPa and 900–1400 °C [56] since Archean, whereas the carbonatitic melts are considered as the most probable carbon source and medium for their crystallization [27,28,57,58], while other media for diamond crystallization are also known [59–63].

The melting along the CaCO_3 – MgCO_3 join extends from 1660 °C (CaCO_3) to 1780 °C (MgCO_3) through a minimum at 1400 °C and 62 mol% CaCO_3 [35] (Figure 6). Consequently, monomineralic inclusions of MgCO_3 , CaCO_3 , and $\text{CaMg}(\text{CO}_3)_2$ in diamonds must be entrapped as minerals, because their melting points exceed the growth temperatures of most lithospheric diamonds (Figure 9).

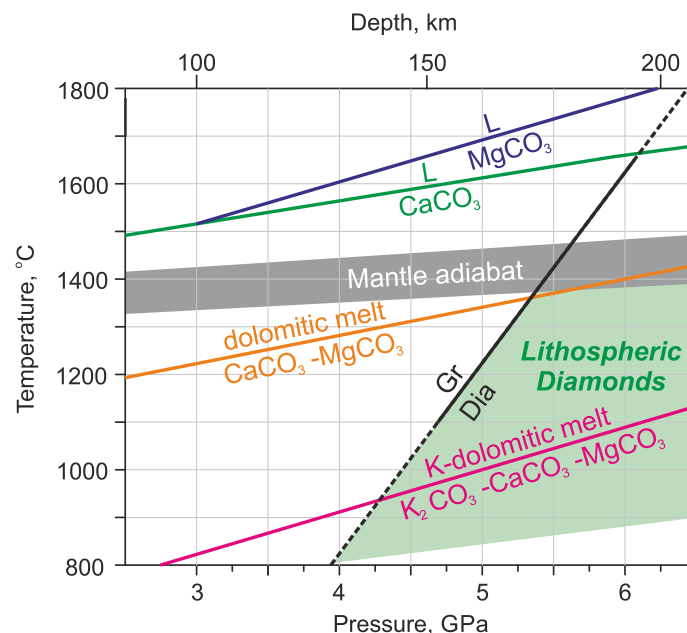


Figure 9. P – T plot illustrating solidus of the K_2CO_3 – CaCO_3 – MgCO_3 and CaCO_3 – MgCO_3 systems and melting curves of CaCO_3 and MgCO_3 [35] compared with mantle adiabat [64] and P – T range of diamond growth in the lithospheric mantle [56]. Gr/Dia—the equilibrium boundary between diamond and graphite [65].

Jablon and Navon [28] discovered K-rich carbonate inclusions of a few hundred nanometers in size entrapped along the twinning plane of macles formed by clear octahedral diamond crystals. The electron probe micro-analyzer (EPMA) revealed that some of these inclusions resemble $\text{K}_2(\text{Mg}, \text{Ca})(\text{CO}_3)_2$ with $\text{Ca}\# = 20$ –43. Our results suggest that these inclusions could be formed in the diamond stability field because at lower pressure, the $\text{K}_2\text{Ca}(\text{CO}_3)_2$ solubility in the $\text{K}_2(\text{Mg}, \text{Ca})(\text{CO}_3)_2$ decreases [37]. The temperature of the entrapment has to be restricted by 1100 °C because at 100 °C higher and lower temperatures the $\text{K}_2\text{Ca}(\text{CO}_3)_2$ content decreases below 10–20 mol% (Figure 5b,f and Tables S2, S6 and S7). Thus, the $\text{Ca}\#$ of about 40 of the $\text{K}_2(\text{Mg}, \text{Ca})(\text{CO}_3)_2$ compound found as single-phase inclusions in diamond implies that its crystallization under the P – T conditions of 6 GPa and 1100 °C, corresponding to the base of the continental lithospheric mantle. However, the further entrapment of diamond by the hot kimberlite magma (1400–1500 °C) [66,67] implies the remelting of the $\text{K}_2(\text{Mg}, \text{Ca})(\text{CO}_3)_2$ compound and its repeated crystallization during kimberlite magma emplacement.

Logvinova et al. [27] identified $\text{K}_2\text{Ca}(\text{CO}_3)_2$ bütschliite within 30 μm carbonate inclusion in a gem-quality octahedral diamond crystal from Sytykanskaya kimberlite pipe (Yakutia). Bütschliite was found in coexistence with dolomite and $\text{Na}_2\text{Mg}(\text{CO}_3)_2$ eitelite. The present results on KCM (Figure 5a,b) and data on NCM [44,45] indicate that neither bütschliite nor eitelite can coexist with dolomite under the P – T conditions of diamond crystallization in the lithospheric mantle (Figure 5). This led to the conclusion that at the time of entrapment, the inclusion material was an alkali-bearing dolomitic melt and that bütschliite is a daughter phase [27].

Although high-pressure carbonates, $\text{K}_8\text{Ca}_3(\text{CO}_3)_7$ and $\text{K}_2\text{Ca}_3(\text{CO}_3)_4$ have not yet been found in diamonds, their high melting points, >1200 and >1300 °C, respectively, do not exclude the possibility of their co-crystallization with diamond and their entrapment as mono- and polymineral inclusions (Figure 6).

4.6. Thermal Stability of Carbonatitic Melts vs. Alkalinity

At 6 GPa, the K_2CO_3 – $CaCO_3$ – $MgCO_3$ system starts to melt near 1100 °C (Figure 8b). This temperature corresponds to the majority of the temperature estimations for peridotitic and eclogitic diamonds [56] and coincides with the continental geotherm with the heat flow of 35 mW/m² [68]. The present results suggest that under the P – T conditions of the continental lithosphere (1100–1200 °C at 6 GPa corresponding to a depth of 200 km), the carbonatitic melt must be alkali-rich. This is consistent with the potassium-rich composition of the most carbonatitic micro inclusions in natural diamonds (Figure 10).

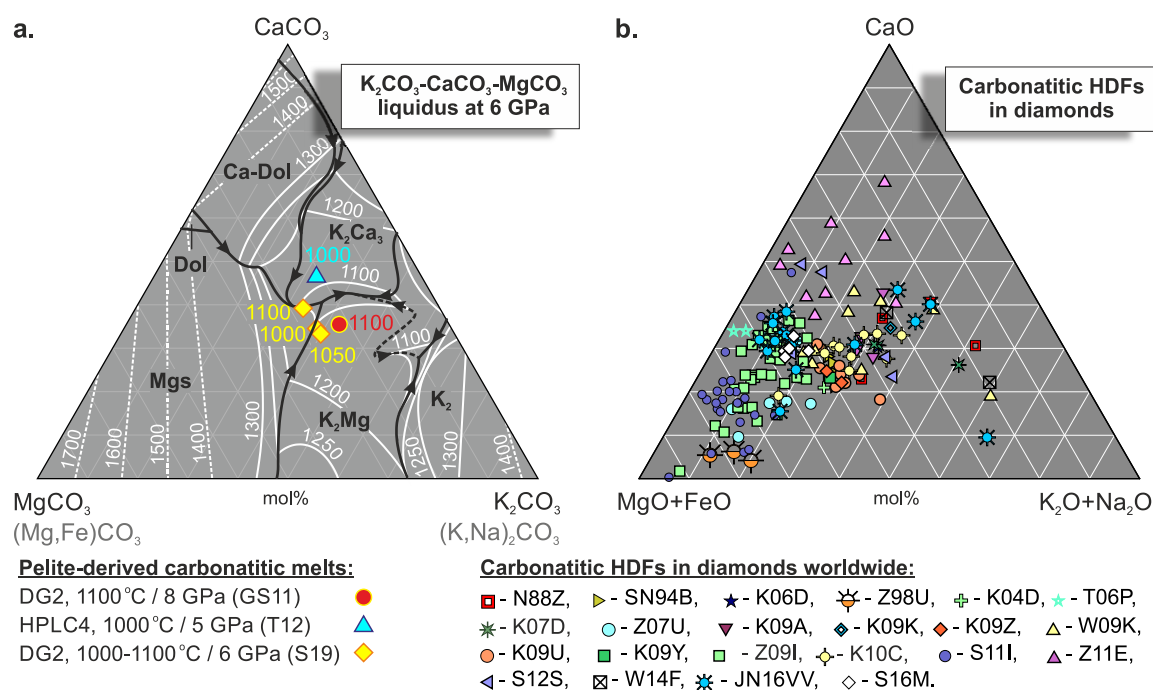


Figure 10. Comparison of the liquidus relationships established in the K_2CO_3 – $CaCO_3$ – $MgCO_3$ system with the compositions of pelite-derived melts (a) and carbonatitic HDFs in diamonds worldwide (b). N88Z—fibrous (cubic and coated octahedral) diamonds from Zaire and Botswana [18]; SN94B—fibrous diamonds with cubic morphology from Jwaneng, Botswana [19]; Z98U—K–Cr-rich aluminosilicate melt inclusions (up to 150 μ m in size) in ‘monocrystalline’ octahedral diamonds of peridotitic suite from Udachnaya kimberlite pipe [69], K04D—a coated diamond from the Diavik mine in Canada containing peridotitic minerals [70]; K06D—fibrous (cubic and coated octahedral) diamonds from the Diavik mine in Canada and the Yubileynaya mine in Russia [71]; T06P—coated diamonds (eclogitic and peridotitic) from the Panda kimberlite in Canada [25]; K07D—fibrous diamonds from the Diavik mine, Canada [72]; Z07U—cuboid fibrous diamonds from the Udachnaya kimberlite, Russia [73]; K09A, K09K, K09U, K09Y, K09Z—fibrous diamonds with cubic morphology from the Aykhal Komsomolskaya, Udachnaya, Yubileynaya, Zarnitsa kimberlite pipes, Russia [21]; W09K—coated octahedral diamonds from Kankan, Guinea [22]; Z09I—cuboid diamonds with fibrous inner zone from Internatsional’naya kimberlite pipe, Russia [20]; S11I—cloudy diamonds from the Internatsional’naya pipe, Russia [74]; Z11E—fibrous diamonds with cubic and semi rounded morphology from the Ebelyakh River placer deposits, Russia [75]; S12S—fibrous diamonds from the 2.701–2.697 Ga Wawa metaconglomerate, Canada [76]; W14F—a coated diamond from Finch mine, South Africa [77]. JN16VV—along (111) twinning surfaces in ‘monocrystalline’ octahedral diamonds of peridotitic suite from South Africa’s Venetia and Voorspoed mines [28]; S16M—cloudy diamonds from the Mir kimberlite pipe, Russia [23].

In contrast to alkali-rich carbonates, alkali-poor carbonates do not experience a full melting under the P – T conditions of the continental geotherm. The melting of Ca–Mg–Fe carbonates [35,78,79] is possible under the temperatures of the convective mantle in asthenosphere, 1450–1500 °C at a depth

of 200 km [64], or at the base of lithospheric mantle under ‘kinked’ geotherm (≥ 1350 °C) developed presumably due to mantle plume activity [80–83]. There is direct evidence of the formation of such melts, namely, kimberlite-associated diamondiferous magnesiocarbonatites [84].

4.7. Daughter Carbonate Minerals, Which Can Be Expected in Diamond Inclusions

Most of the carbonatitic inclusions in diamonds fall into the primary crystallization field of Mgs. Slow cooling of these inclusions, which could occur in hypabyssal conditions, should cause crystallization of Mgs. This shifts the residual melt composition toward the K-rich eutectic one (E¹) and yields precipitation of $K_2Mg + K_2Ca_3 + K_8Ca_3$ at the final stage of crystallization (Figure 7d). If we consider a possible pressure drop upon cooling, the daughter phases may also include K_2Ca_2 , K_2Ca , and K_2 (Figure 7a,b).

Explosive eruption of kimberlite magma implies a rapid cooling of diamonds and micro inclusions therein. In this case, the following assemblages of carbonate phases can be formed: Mgs + Arg + K_2Mg , Arg + $K_2Ca_3 + K_2Mg$, $K_2Mg + K_2Ca + K_2Ca_3$, and $K_2 + K_2Mg + K_2Ca$ (Figure 7c). A pressure drop upon cooling can also yield an appearance of the following assemblages Mgs + $K_2Ca + K_2Mg$, Mgs + $K_2Ca + K_2Ca_2$, and Mgs + $K_2Ca_2 + Dol$ (Figure 7a).

4.8. Comparison with Carbonated Pelite-Derived Melts

Neither peridotites nor eclogites with the natural abundance of K_2O can yield formation of K-rich melts [85–87]. On the other hand, partial melting of carbonated pelites at 5–8 GPa and 1000–1100 °C yields K-rich dolomitic melts [29–31], which resemble a minimum on the K_2CO_3 – $CaCO_3$ – $MgCO_3$ liquidus established in the present study (Figure 10a). This suggests that the melting behavior of the $KAlSi_3O_8$ – $CaMg(CO_3)_2$ system, controlling carbonated pelite solidus, is essentially the same as that established here in the K_2CO_3 – $CaCO_3$ – $MgCO_3$ system at 6 GPa.

5. Conclusions

Phase relations in the K_2CO_3 – $CaCO_3$ – $MgCO_3$ system have been studied at 6 GPa and 900–1300 °C using Kawai-type multianvil press. At the subsolidus conditions in experiments at 900 and 1000 °C, three intermediate compounds $K_2Ca_3(CO_3)_4$ (Ca# ≥ 97), $K_2Ca(CO_3)_2$ bütschliite (Ca# ≥ 58), and $K_2Mg(CO_3)_2$ (Ca# ≤ 10) were established. A miscibility gap between $K_2Ca(CO_3)_2$ and $K_2Mg(CO_3)_2$ suggest that their crystal structures differ at 6 GPa. $K_2Ca(CO_3)_2$ (Ca# ≤ 28) disappear above 1000 °C to produce $K_2Ca_3(CO_3)_4 + K_8Ca_3(CO_3)_7 + K_2Mg(CO_3)_2$.

The system has four ternary peritectic points and two minima on the liquidus at about 1090 °C corresponding to ternary eutectic points. The eutectics are controlled by the following melting reactions: $K_2Ca_3(CO_3)_4 + K_8Ca_3(CO_3)_7 + K_2Mg(CO_3)_2 \rightarrow [40K_2CO_3 \cdot 60(Ca_{0.70}Mg_{0.30})CO_3]$ (1st eutectic melt) and $K_8Ca_3(CO_3)_7 + K_2CO_3 + K_2Mg(CO_3)_2 \rightarrow [62K_2CO_3 \cdot 38(Ca_{0.73}Mg_{0.27})CO_3]$ (2nd eutectic melt). The peritectic points are controlled by the following reactions: $K_2Ca_3(CO_3)_4 + K_2Mg(CO_3)_2 \rightarrow Mgs + liquid$ (P¹), at 1075 ± 25 °C; $K_2Ca_3(CO_3)_4 + magnesite \rightarrow Ca-Dol + liquid$ (P²), at 1150 ± 50 °C; $K_2Ca_3(CO_3)_4 + Ca-dolomite \rightarrow Arg + liquid$ (P³), at 1150 ± 50 °C; $Ca-dolomite + magnesite \rightarrow dolomite + liquid$ (P⁴), at 1350 ± 50 °C.

The liquidus projection of the studied ternary system has eight primary crystallization phase regions for magnesite, aragonite, dolomite, Ca-dolomite, $K_2Ca_3(CO_3)_4$, $K_8Ca_3(CO_3)_7$, $K_2Mg(CO_3)_2$ and K_2CO_3 . The temperature increase is accompanied by the sequential disappearance of crystalline phases in the following sequence: $K_8Ca_3(CO_3)_7$ (1220 °C) \rightarrow $K_2Mg(CO_3)_2$ (1250 °C) \rightarrow $K_2Ca_3(CO_3)_4$ (1350 °C) \rightarrow K_2CO_3 (1425 °C) \rightarrow dolomite (1450 °C) \rightarrow $CaCO_3$ (1660 °C) \rightarrow magnesite (1780 °C).

The high alkali content in the carbonate melt is a necessary condition for its existence under geothermal conditions of the continental lithosphere. The obtained results indicate that at 6 GPa and 1100–1200 °C corresponding to the base of the continental lithospheric mantle, the K-Ca-Mg carbonate melts must contain 20–40 mol% K_2CO_3 , otherwise, it will simply freeze.

Supplementary Materials: Figure S1 and Tables S1–S10 are available online at <http://www.mdpi.com/2075-163X/9/9/558/s1>, Figure S1: BSE images illustrating the damage of K_2CO_3 -bearing samples by atmospheric humidity, Table S1: Composition (mol %) of the run products in the K_2CO_3 – $CaCO_3$ – $MgCO_3$ ternary system at 900 °C, 6 GPa and run duration of 48 h. (run no. D075); Table S2: Composition (mol %) of the run products in the K_2CO_3 – $CaCO_3$ – $MgCO_3$ ternary system at 1000 °C, 6 GPa and run duration of 24 h. (run no. D077); Table S3: Composition (mol %) of the run products in the K_2CO_3 – $CaCO_3$ – $MgCO_3$ ternary system at 1100 °C, 6 GPa and run duration of 47 h. (run no. D078); Table S4: Composition (mol %) of the run products in the K_2CO_3 – $CaCO_3$ – $MgCO_3$ ternary system at 1100 °C, 6 GPa and run duration of 6 h. (run no. D158); Table S5: Composition (mol %) of the run products in the K_2CO_3 – $CaCO_3$ – $MgCO_3$ ternary system at 1200 °C, 6 GPa and run duration of 25 h. (run no. D079); Table S6: Composition (mol %) of the run products in the K_2CO_3 – $CaCO_3$ – $MgCO_3$ ternary system at 1200 °C, 6 GPa and run duration of 4 h. (run no. D162); Table S7: Composition (mol %) of the run products in the K_2CO_3 – $CaCO_3$ – $MgCO_3$ ternary system at 1200 °C, 6 GPa and run duration of 10 h. (run no. D172); Table S8: Composition (mol %) of the run products in the K_2CO_3 – $CaCO_3$ – $MgCO_3$ ternary system at 1250 °C, 6 GPa and run duration of 4 h. (run no. D169); Table S9: Composition (mol %) of the run products in the K_2CO_3 – $CaCO_3$ – $MgCO_3$ ternary system at 1300 °C, 6 GPa and run duration of 2 h. (run no. D170); Table S10: Calculation of the eutectic reactions.

Author Contributions: Conceptualization, A.S.; methodology, A.S. and K.D.L.; validation, A.S. and A.V.A.; formal analysis, A.V.A. and I.V.P.; investigation, A.V.A.; resources, K.D.L. and A.S.; data curation, A.V.A.; writing—original draft preparation, A.S. and A.V.A.; writing—review and editing, A.S.; visualization, A.V.A. and A.S.; supervision, A.S.; project administration, A.V.A. and A.S.; funding acquisition, A.S. and K.D.L.

Funding: The work is done on the state assignment of IGM SB RAS.

Acknowledgments: The SEM and EDS studies of experimental samples were performed in the Analytical Center for multi-elemental and isotope research SB RAS. We are grateful to two anonymous referees for comments that helped to improve the manuscript and N.S. Karmanov and A.T. Titov for help in analytical work.

Conflicts of Interest: The authors declare no conflict of interest. The funders had no role in the design of the study; in the collection, analyses, or interpretation of data; in the writing of the manuscript, and in the decision to publish the results.

Nomenclature

Arg = aragonite,	$K_2 = K_2CO_3,$
Cal = calcite,	$K_8Ca_3 = K_8Ca_3(CO_3)_7,$
Mg-Cal = Mg-bearing calcite,	$K_2Ca = K_2Ca(CO_3)_2,$
Ca-Dol = Ca-rich dolomite,	$K_2Ca_2 = K_2Ca_2(CO_3)_3,$
Dol = dolomite,	$K_2Ca_3 = K_2Ca_3(CO_3)_4,$
Mgs = magnesite,	$K_2Mg = K_2Mg(CO_3)_2.$
L = liquid,	

References

1. Pyle, J.M.; Haggerty, S.E. Silicate-carbonate liquid immiscibility in upper-mantle eclogites: implications for natrosilicic and carbonatitic conjugate melts. *Geochim. Cosmochim. Acta* **1994**, *58*, 2997–3011. [[CrossRef](#)]
2. Kogarko, L.N.; Henderson, C.M.B.; Pacheco, H. Primary Ca-rich carbonatite magma and carbonate-silicate-sulphide liquid immiscibility in the upper mantle. *Contrib. Mineral. Petrol.* **1995**, *121*, 267–274. [[CrossRef](#)]
3. Ionov, D. Trace element composition of mantle-derived carbonates and coexisting phases in peridotite xenoliths from alkali basalts. *J. Petrol.* **1998**, *39*, 1931–1941. [[CrossRef](#)]
4. Nikolenko, E.I.; Sharygin, I.S.; Alifirova, T.A.; Korsakov, A.V.; Zelenovskiy, P.S.; Shur, V.Y. Graphite-bearing mineral assemblages in the mantle beneath Central Aldan superterrane of North Asian craton: combined confocal micro-Raman and electron microprobe characterization. *J. Raman Spectrosc.* **2017**, *48*, 1597–1605. [[CrossRef](#)]
5. Rezvukhin, D.I.; Malkovets, V.G.; Sharygin, I.S.; Tretiakova, I.G.; Griffin, W.L.; O'Reilly, S.Y. Inclusions of crichtonite-group minerals in Cr-pyropes from the Internatsionalnaya kimberlite pipe, Siberian Craton: Crystal chemistry, parageneses and relationships to mantle metasomatism. *Lithos* **2018**, *308*, 181–195. [[CrossRef](#)]
6. Meyer, H.O.A.; McCallum, M.E. Mineral inclusions in diamonds from the Sloan kimberlites, Colorado. *J. Geology* **1986**, *94*, 600–612. [[CrossRef](#)]
7. Bulanova, G.P.; Pavlova, L.P. Magnesite peridotite assemblage in diamond from the Mir pipe. *Dokl. Akad. Nauk SSSR* **1987**, *295*, 1452–1456.

8. Wang, A.; Pasteris, J.D.; Meyer, H.O.A.; DeleDuboi, M.L. Magnesite-bearing inclusion assemblage in natural diamond. *Earth Planet. Sci. Lett.* **1996**, *141*, 293–306. [[CrossRef](#)]
9. Stachel, T.; Harris, J.W.; Brey, G.P. Rare and unusual mineral inclusions in diamonds from Mwadui, Tanzania. *Contrib. Mineral. Petrol.* **1998**, *132*, 34–47. [[CrossRef](#)]
10. Brenker, F.E.; Vollmer, C.; Vincze, L.; Vekemans, B.; Szymanski, A.; Janssens, K.; Szaloki, I.; Nasdala, L.; Joswig, W.; Kaminsky, F. Carbonates from the lower part of transition zone or even the lower mantle. *Earth Planet. Sci. Lett.* **2007**, *260*, 1–9. [[CrossRef](#)]
11. Sobolev, N.V.; Logvinova, A.M.; Efimova, E.S. Syngenetic phlogopite inclusions in kimberlite-hosted diamonds: implications for role of volatiles in diamond formation. *Russ. Geol. Geophys.* **2009**, *50*, 1234–1248. [[CrossRef](#)]
12. Logvinova, A.M.; Wirth, R.; Zedgenizov, D.A.; Taylor, L.A. Carbonate–Silicate–Sulfide Polyphase Inclusion in Diamond from the Komsomolskaya Kimberlite Pipe, Yakutia. *Geochem. Int.* **2018**, *56*, 283–291. [[CrossRef](#)]
13. Zedgenizov, D.A.; Shatskiy, A.; Ragozin, A.L.; Kagi, H.; Shatsky, V.S. Merwinite in diamond from São Luis, Brazil: A new mineral of the Ca-rich mantle environment. *Am. Mineral.* **2014**, *99*, 547–550. [[CrossRef](#)]
14. Sobolev, N.V.; Shatsky, V.S. Diamond inclusions in garnets from metamorphic rocks: a new environment for diamond formation. *Nature* **1990**, *343*, 742–746. [[CrossRef](#)]
15. Shatsky, V.S.; Sobolev, N.V.; Vavilov, M.A. Diamond-bearing metamorphic rocks from the Kokchetav massif (Northern Kazakhstan). In *Ultrahigh Pressure Metamorphism*; Coleman, R.G., Wang, X., Eds.; Cambridge University Press: Cambridge, UK, 1995; pp. 427–455.
16. Dobrzhinetskaya, L.F.; Wirth, R.; Green, H.W. Nanometric inclusions of carbonates in Kokchetav diamonds from Kazakhstan: A new constraint for the depth of metamorphic diamond crystallization. *Earth Planet. Sci. Lett.* **2006**, *243*, 85–93. [[CrossRef](#)]
17. Korsakov, A.V.; Hermann, J. Silicate and carbonate melt inclusions associated with diamonds in deeply subducted carbonate rocks. *Earth Planet. Sci. Lett.* **2006**, *241*, 104–118. [[CrossRef](#)]
18. Navon, O.; Hutcheon, I.; Rossman, G.; Wasserburg, G. Mantle-derived fluids in diamond micro-inclusions. *Nature* **1988**, *335*, 784–789. [[CrossRef](#)]
19. Schrauder, M.; Navon, O. Hydrous and carbonatitic mantle fluids in fibrous diamonds from Jwaneng, Botswana. *Geochim. Cosmochim. Acta* **1994**, *58*, 761–771. [[CrossRef](#)]
20. Zedgenizov, D.A.; Ragozin, A.L.; Shatsky, V.S.; Araujo, D.; Griffin, W.L.; Kagi, H. Mg and Fe-rich carbonate-silicate high-density fluids in cuboid diamonds from the Internationalnaya kimberlite pipe (Yakutia). *Lithos* **2009**, *112*, 638–647. [[CrossRef](#)]
21. Klein-BenDavid, O.; Logvinova, A.M.; Schrauder, M.; Spetius, Z.V.; Weiss, Y.; Hauri, E.H.; Kaminsky, F.V.; Sobolev, N.V.; Navon, O. High-Mg carbonatitic micro inclusions in some Yakutian diamonds—A new type of diamond-forming fluid. *Lithos* **2009**, *112*, 648–659. [[CrossRef](#)]
22. Weiss, Y.; Kessel, R.; Griffin, W.L.; Kiflawi, I.; Klein-BenDavid, O.; Bell, D.R.; Harris, J.W.; Navon, O. A new model for the evolution of diamond-forming fluids: Evidence from microinclusion-bearing diamonds from Kankan, Guinea. *Lithos* **2009**, *112*, 660–674. [[CrossRef](#)]
23. Skuzovatov, S.; Zedgenizov, D.; Howell, D.; Griffin, W.L. Various growth environments of cloudy diamonds from the Malobotuobia kimberlite field (Siberian craton). *Lithos* **2016**, *265*, 96–107. [[CrossRef](#)]
24. Logvinova, A.M.; Wirth, R.; Tomilenko, A.A.; Afanas'ev, V.P.; Sobolev, N.V. The phase composition of crystal-fluid nanoinclusions in alluvial diamonds in the northeastern Siberian Platform. *Russ. Geol. Geophys.* **2011**, *52*, 1286–1297. [[CrossRef](#)]
25. Tomlinson, E.L.; Jones, A.P.; Harris, J.W. Co-existing fluid and silicate inclusions in mantle diamond. *Earth Planet. Sci. Lett.* **2006**, *250*, 581–595. [[CrossRef](#)]
26. Navon, O. High internal pressure in diamond fluid inclusions determined by infrared absorption. *Nature* **1991**, *353*, 746–748. [[CrossRef](#)]
27. Logvinova, A.M.; Shatskiy, A.; Wirth, R.; Ugap'eva, S.S.; Sobolev, N.V. Carbonatite melt in type Ia gem diamond. *Lithos* **2019**, *342-343*, 463–467. [[CrossRef](#)]
28. Jablon, B.M.; Navon, O. Most diamonds were created equal. *Earth Planet. Sci. Lett.* **2016**, *443*, 41–47. [[CrossRef](#)]
29. Tsuno, K.; Dasgupta, R.; Danielson, L.; Richter, K. Flux of carbonate melt from deeply subducted pelitic sediments: Geophysical and geochemical implications for the source of Central American volcanic arc. *Geophys. Res. Lett.* **2012**, *39*. [[CrossRef](#)]

30. Grassi, D.; Schmidt, M.W. Melting of carbonated pelites at 8–13 GPa: Generating K-rich carbonatites for mantle metasomatism. *Contrib. Mineral. Petrol.* **2011**, *162*, 169–191. [[CrossRef](#)]
31. Shatskiy, A.; Arefiev, A.V.; Podborodnikov, I.V.; Litasov, K.D. Origin of K-rich diamond-forming immiscible melts and CO₂ fluid via partial melting of carbonated pelites at a depth of 180–200 km. *Gondwana Res.* **2019**, *75*, 154–171. [[CrossRef](#)]
32. Litasov, K.D.; Shatskiy, A.; Ohtani, E.; Yaxley, G.M. The solidus of alkaline carbonatite in the deep mantle. *Geology* **2013**, *41*, 79–82. [[CrossRef](#)]
33. Shatskiy, A.; Litasov, K.D.; Palyanov, Y.N.; Ohtani, E. Phase relations on the K₂CO₃–CaCO₃–MgCO₃ join at 6 GPa and 900–1400 °C: Implications for incipient melting in carbonated mantle domains. *Am. Mineral.* **2016**, *101*, 437–447. [[CrossRef](#)]
34. Shatskiy, A.; Litasov, K.D.; Terasaki, H.; Katsura, T.; Ohtani, E. Performance of semi-sintered ceramics as pressure-transmitting media up to 30 GPa. *High Press. Res.* **2010**, *30*, 443–450. [[CrossRef](#)]
35. Shatskiy, A.; Podborodnikov, I.V.; Arefiev, A.V.; Minin, D.A.; Chanyshv, A.D.; Litasov, K.D. Revision of the CaCO₃–MgCO₃ phase diagram at 3 and 6 GPa. *Am. Mineral.* **2018**, *103*, 441–452. [[CrossRef](#)]
36. Shatskiy, A.; Sharygin, I.S.; Gavryushkin, P.N.; Litasov, K.D.; Borzdov, Y.M.; Shcherbakova, A.V.; Higo, Y.; Funakoshi, K.-I.; Palyanov, Y.N.; Ohtani, E. The system K₂CO₃–MgCO₃ at 6 GPa and 900–1450 °C. *Am. Mineral.* **2013**, *98*, 1593–1603. [[CrossRef](#)]
37. Arefiev, A.V.; Shatskiy, A.; Podborodnikov, I.V.; Behtenova, A.; Litasov, K.D. The system K₂CO₃–CaCO₃–MgCO₃ at 3 GPa: Implications for carbonatite melt compositions in the subcontinental lithospheric mantle. *Minerals* **2019**, *9*, 296. [[CrossRef](#)]
38. Shatskiy, A.; Borzdov, Y.M.; Litasov, K.D.; Sharygin, I.S.; Palyanov, Y.N.; Ohtani, E. Phase relationships in the system K₂CO₃–CaCO₃ at 6 GPa and 900–1450 °C. *Am. Mineral.* **2015**, *100*, 223–232. [[CrossRef](#)]
39. Arefiev, A.V.; Shatskiy, A.; Podborodnikov, I.V.; Rashchenko, S.V.; Chanyshv, A.D.; Litasov, K.D. The system K₂CO₃–CaCO₃ at 3 GPa: Link between phase relations and variety of K–Ca double carbonates at ≤ 0.1 and 6 GPa. *Phys. Chem. Miner.* **2019**, *46*, 229–244. [[CrossRef](#)]
40. Arefiev, A.V.; Shatskiy, A.; Podborodnikov, I.V.; Litasov, K.D. Melting and subsolidus phase relations in the system K₂CO₃–MgCO₃ at 3 GPa. *High Press. Res.* **2018**, *38*, 422–439. [[CrossRef](#)]
41. Cooper, A.F.; Gittins, J.; Tuttle, O.F. The system Na₂CO₃–K₂CO₃–CaCO₃ at 1 kilobar and its significance in carbonatite petrogenesis. *Am. J. Sci.* **1975**, *275*, 534–560. [[CrossRef](#)]
42. Ragon, S.E.; Datta, R.K.; Roy, D.M.; Tuttle, O.F. The system potassium carbonate–magnesium carbonate. *J. Phys. Chem.* **1966**, *70*, 3360–3361. [[CrossRef](#)]
43. Arefiev, A.V.; Podborodnikov, I.V.; Shatskiy, A.F.; Litasov, K.D. Synthesis and Raman spectra of K–Ca double carbonates: K₂Ca(CO₃)₂ bütschliite, fairchildite and K₂Ca₂(CO₃)₃ at 1 atm. *Geochem. Int.* **2019**, *57*, 981–987. [[CrossRef](#)]
44. Podborodnikov, I.V.; Shatskiy, A.; Arefiev, A.V.; Bekhtenova, A.; Litasov, K.D. New data on the system Na₂CO₃–CaCO₃–MgCO₃ at 6 GPa with implications to the composition and stability of carbonatite melts at the base of continental lithosphere. *Chem. Geol.* **2019**, *515*, 50–60. [[CrossRef](#)]
45. Podborodnikov, I.V.; Shatskiy, A.; Arefiev, A.V.; Litasov, K.D. Phase relations in the system Na₂CO₃–CaCO₃–MgCO₃ at 3 GPa with implications for carbonatite genesis and evolution. *Lithos* **2019**, *330–331*, 74–89. [[CrossRef](#)]
46. Eitel, W.; Skaliks, W. Ueber einige doppelcarbonate der alkalien und erdalkalien. *Z. Anorg. Allg. Chem.* **1929**, *183*, 263–286. [[CrossRef](#)]
47. Brey, G.P.; Bulatov, V.K.; Girmis, A.V. Melting of K-rich carbonated peridotite at 6–10 GPa and the stability of K-phases in the upper mantle. *Chem. Geol.* **2011**, *281*, 333–342. [[CrossRef](#)]
48. Pabst, A. Synthesis, properties, and structure of K₂Ca(CO₃)₂, bütschliite. *Am. Mineral.* **1974**, *59*, 353–358.
49. Hesse, K.-F.; Simons, B. Crystalstructure of synthetic K₂Mg(CO₃)₂. *Z. Krist.* **1982**, *161*, 289–292. [[CrossRef](#)]
50. Golubkova, A.; Merlini, M.; Schmidt, M.W. Crystal structure, high-pressure, and high-temperature behavior of carbonates in the K₂Mg(CO₃)₂–Na₂Mg(CO₃)₂ join. *Am. Mineral.* **2015**, *100*, 2458–2467. [[CrossRef](#)]
51. Logvinova, A.; Zedgenizov, D.; Wirth, R. Specific Multiphase assemblages of carbonatitic and Al-rich silicic diamond-forming fluids/melts: TEM observation of micro inclusions in cuboid diamonds from the placers of northeastern Siberian Craton. *Minerals* **2019**, *9*, 50. [[CrossRef](#)]
52. Stachel, T.; Harris, J.W.; Brey, G.P.; Joswig, W. Kankan diamonds (Guinea) II: Lower mantle inclusion parageneses. *Contrib. Mineral. Petrol.* **2000**, *140*, 16–27. [[CrossRef](#)]

53. Kaminsky, F.; Wirth, R.; Matsyuk, S.; Schreiber, A.; Thomas, R. Nyerereite and nahcolite inclusions in diamond: Evidence for lower-mantle carbonatitic magmas. *Mineral. Mag.* **2009**, *73*, 797–816. [[CrossRef](#)]
54. Smith, E.M.; Kopylova, M.G.; Dubrovinsky, L.; Navon, O.; Ryder, J.; Tomlinson, E.L. Transmission X-ray diffraction as a new tool for diamond fluid inclusion studies. *Mineral. Mag.* **2011**, *75*, 2657–2675. [[CrossRef](#)]
55. Kaminsky, F.V.; Wirth, R.; Schreiber, A. Carbonatitic inclusions in deep mantle diamond from Juina, Brazil: New minerals in the carbonate-halide association. *Can. Mineral.* **2013**, *51*, 669–688. [[CrossRef](#)]
56. Stachel, T.; Luth, R.W. Diamond formation—Where, when and how? *Lithos* **2015**, *220*, 200–220. [[CrossRef](#)]
57. Pal'yanov, Y.N.; Sokol, A.G.; Borzdov, Y.M.; Khokhryakov, A.F.; Sobolev, N.V. Diamond formation from mantle carbonate fluids. *Nature* **1999**, *400*, 417–418. [[CrossRef](#)]
58. Palyanov, Y.N.; Bataleva, Y.V.; Sokol, A.G.; Borzdov, Y.M.; Kupriyanov, I.N.; Reutsky, V.N.; Sobolev, N.V. Mantle–slab interaction and redox mechanism of diamond formation. *Proc. Natl. Acad. Sci. USA* **2013**, *110*, 20408–20413. [[CrossRef](#)]
59. Girnis, A.V.; Brey, G.P.; Bulatov, V.K.; Höfer, H.E.; Woodland, A.B. Graphite to diamond transformation during sediment–peridotite interaction at 7.5 and 10.5 GPa. *Lithos* **2018**, *310*, 302–313. [[CrossRef](#)]
60. Wang, Y.; Kanda, H. Growth of HPHT diamonds in alkali halides: possible effects of oxygen contamination. *Diam. Relat. Mater.* **1998**, *7*, 57–63. [[CrossRef](#)]
61. Arima, M.; Nakayama, K.; Akaishi, M.; Yamaoka, S.; Kanda, H. Crystallization of diamond from a silicate melt of kimberlite composition in high-pressure and high-temperature experiments. *Geology* **1993**, *21*, 968–970. [[CrossRef](#)]
62. Akaishi, M. New nonmetallic catalysts for the synthesis of high-pressure, high-temperature diamond. *Diam. Relat. Mater.* **1993**, *2*, 183–189. [[CrossRef](#)]
63. Palyanov, Y.N.; Sokol, A.G. The effect of composition of mantle fluids/melts on diamond formation processes. *Lithos* **2009**, *112*, 690–700. [[CrossRef](#)]
64. Katsura, T.; Yoneda, A.; Yamazaki, D.; Yoshino, T.; Ito, E. Adiabatic temperature profile in the mantle. *Phys. Earth Planet. Inter.* **2010**, *183*, 212–218. [[CrossRef](#)]
65. Kennedy, C.S.; Kennedy, G.C. The equilibrium boundary between graphite and diamond. *J. Geophys. Res.* **1976**, *81*, 2467–2470. [[CrossRef](#)]
66. Shatskiy, A.; Litasov, K.D.; Sharygin, I.S.; Ohtani, E. Composition of primary kimberlite melt in a garnet lherzolite mantle source: Constraints from melting phase relations in anhydrous Udachnaya-East kimberlite with variable CO₂ content at 6.5 GPa. *Gondwana Res.* **2017**, *45*, 208–227. [[CrossRef](#)]
67. Kavanagh, J.L.; Sparks, R.S.J. Temperature changes in ascending kimberlite magma. *Earth Planet. Sci. Lett.* **2009**, *286*, 404–413. [[CrossRef](#)]
68. Pollack, H.N.; Chapman, D.S. On the regional variation of heat flow, geotherms, and lithospheric thickness. *Tectonophysics* **1977**, *38*, 279–296. [[CrossRef](#)]
69. Zedgenizov, D.A.; Logvinova, A.M.; Shatskii, V.S.; Sobolev, N.V. Inclusions in microdiamonds from some kimberlite diatremes of Yakutia. *Dokl. Earth Sci.* **1998**, *359*, 204–208.
70. Klein-BenDavid, O.; Izraeli, E.S.; Hauri, E.; Navon, O. Mantle fluid evolution—A tale of one diamond. *Lithos* **2004**, *77*, 243–253. [[CrossRef](#)]
71. Klein-BenDavid, O.; Wirth, R.; Navon, O. TEM imaging and analysis of micro inclusions in diamonds: A close look at diamond-growing fluids. *Am. Mineral.* **2006**, *91*, 353–365. [[CrossRef](#)]
72. Klein-BenDavid, O.; Izraeli, E.S.; Hauri, E.; Navon, O. Fluid inclusions in diamonds from the Diavik mine, Canada and the evolution of diamond-forming fluids. *Geochim. Cosmochim. Acta* **2007**, *71*, 723–744. [[CrossRef](#)]
73. Zedgenizov, D.A.; Rege, S.; Griffin, W.L.; Kagi, H.; Shatsky, V.S. Composition of trapped fluids in cuboid fibrous diamonds from the Udachnaya kimberlite: LAM-ICPMS analysis. *Chem. Geol.* **2007**, *240*, 151–162. [[CrossRef](#)]
74. Skuzovatov, S.Y.; Zedgenizov, D.A.; Shatsky, V.S.; Ragozin, A.L.; Kuper, K.E. Composition of cloudy micro inclusions in octahedral diamonds from the Internatsional'naya kimberlite pipe (Yakutia). *Russ. Geol. Geophys.* **2011**, *52*, 85–96. [[CrossRef](#)]
75. Zedgenizov, D.A.; Ragozin, A.L.; Shatsky, V.S.; Araujo, D.; Griffin, W.L. Fibrous diamonds from the placers of the northeastern Siberian Platform: carbonate and silicate crystallization media. *Russ. Geol. Geophys.* **2011**, *52*, 1298–1309. [[CrossRef](#)]
76. Smith, E.M.; Kopylova, M.G.; Nowell, G.M.; Pearson, D.G.; Ryder, J. Archean mantle fluids preserved in fibrous diamonds from Wawa, Superior craton. *Geology* **2012**, *40*, 1071–1074. [[CrossRef](#)]

77. Weiss, Y.; Kiflawi, I.; Davies, N.; Navon, O. High-density fluids and the growth of monocrystalline diamonds. *Geochim. Cosmochim. Acta* **2014**, *141*, 145–159. [[CrossRef](#)]
78. Shatskiy, A.; Borzdov, Y.M.; Litasov, K.D.; Kupriyanov, I.N.; Ohtani, E.; Palyanov, Y.N. Phase relations in the system $\text{FeCO}_3\text{-CaCO}_3$ at 6 GPa and 900–1700 °C and its relation to the system $\text{CaCO}_3\text{-FeCO}_3\text{-MgCO}_3$. *Am. Mineral.* **2014**, *99*, 773–785. [[CrossRef](#)]
79. Shatskiy, A.; Litasov, K.D.; Ohtani, E.; Borzdov, Y.M.; Khmelnicov, A.I.; Palyanov, Y.N. Phase relations in the $\text{K}_2\text{CO}_3\text{-FeCO}_3$ and $\text{MgCO}_3\text{-FeCO}_3$ systems at 6 GPa and 900–1700 °C. *Eur. J. Mineral.* **2015**, *27*, 487–499. [[CrossRef](#)]
80. Tychkov, N.S.; Agashev, A.M.; Malygina, E.V.; Nikolenko, E.I.; Pokhilenko, N.P. Thermal perturbations in the lithospheric mantle as evidenced from PT equilibrium conditions of xenoliths from the Udachnaya kimberlite pipe. *Dokl. Earth Sci.* **2014**, *454*, 84–88. [[CrossRef](#)]
81. Agashev, A.M.; Pokhilenko, L.N.; Pokhilenko, N.P.; Shchukina, E.V. Geochemistry of eclogite xenoliths from the Udachnaya Kimberlite Pipe: Section of ancient oceanic crust sampled. *Lithos* **2018**, *314–315*, 187–200. [[CrossRef](#)]
82. Boyd, F.R.; Nixon, P.H. Origins of the ultramafic nodules from some kimberlites of northern Lesotho and the Monastery Mine, South Africa. *Phys. Chem. Earth* **1975**, *9*, 431–454. [[CrossRef](#)]
83. Green, H.W.; Gueguen, Y. Origin of kimberlite pipes by diapiric upwelling in the upper mantle. *Nature* **1974**, *249*, 617–620. [[CrossRef](#)]
84. Agashev, A.M.; Pokhilenko, N.R.; Takazawa, E.; McDonald, J.A.; Vavilov, M.A.; Watanabe, I.; Sobolev, N.V. Primary melting sequence of a deep (>250 km) lithospheric mantle as recorded in the geochemistry of kimberlite-carbonatite assemblages, Snap Lake dyke system, Canada. *Chem. Geol.* **2008**, *255*, 317–328. [[CrossRef](#)]
85. Yaxley, G.M.; Brey, G.P. Phase relations of carbonate-bearing eclogite assemblages from 2.5 to 5.5 GPa: Implications for petrogenesis of carbonatites. *Contrib. Mineral. Petrol.* **2004**, *146*, 606–619. [[CrossRef](#)]
86. Dasgupta, R.; Hirschmann, M.M. Effect of variable carbonate concentration on the solidus of mantle peridotite. *Am. Mineral.* **2007**, *92*, 370–379. [[CrossRef](#)]
87. Brey, G.P.; Bulatov, V.K.; Gurnis, A.V.; Lahaye, Y. Experimental melting of carbonated peridotite at 6–10 GPa. *J. Petrol.* **2008**, *49*, 797–821. [[CrossRef](#)]



© 2019 by the authors. Licensee MDPI, Basel, Switzerland. This article is an open access article distributed under the terms and conditions of the Creative Commons Attribution (CC BY) license (<http://creativecommons.org/licenses/by/4.0/>).